Transcriptional Dynamics Uncover the Role of BNIP3 in Mitophagy during Muscle Remodeling in *Drosophila*

(Running title: BNIP3-mediated mitophagy in fly muscle)

Hiroki Taoka[1,3,#], Tadayoshi Murakawa[2,#], Kawaguchi Kohei[1], Michiko Koizumi[1], Tatsuya Kaminishi[4], Yuriko Sakamaki[5], Kaori Tanaka[6], Akihito Harada[6], Keiichi Inoue[7], Tomotake Kanki[7], Yasuyuki Ohkawa[6], and Naonobu Fujita[1,2,*]

[1] Cell Biology Center, Institute of Integrated Research, Institute of Science Tokyo, 4259 S2-11 Nagatsuta, Midori-ku, Yokohama, Kanagawa 226-8501, Japan.
[2] School of Life Science and Technology, Institute of Science Tokyo, Yokohama, Kanagawa, Japan.
[3] Biological Science Research Laboratories, Kao Corporation, 2606, Akabane, Ichikai, Haga-gun, Tochigi 321-3497, Japan.
[4] Department of Genetics, Graduate School of Medicine, Osaka University, 2-2 Yamadaoka, Suita, Osaka 565-0871, Japan.
[5] Ochanomizu Research Facility (ORF), Bioscience Center, Research Infrastructure Management Center, Institute of Science Tokyo, 1-5-45, Yushima, Bunkyo-ku, Tokyo 113-8510, Japan.
[6] Division of Transcriptomics, Medical Institute of Bioregulation, Kyushu University, 3-1-1, Maida, Higashi-ku, Fukuoka 812-8582, Japan.
[7] Department of Cellular Physiology, Graduate School of Medical Sciences, Kyushu University, 3-1-1 Maida, Higashi-ku, Fukuoka 812-8582, Japan.

[#] These authors equally contributed to this work.
* Corresponding author. Tel: +81 45 924 5131; E-mail: nafujita@cbc.iir.isct.ac.jp

Keywords: Muscle, *Drosophila*, Remodeling, BNIP3, mitochondria, RNA-seq, autophagy

Impact statement: A time-course RNA-seq analysis of muscle remodeling reveals transcriptional dynamics independent of autophagy and highlights the significance of BNIP3 in mitochondrial degradation *in vivo*.

Abbreviations used: APF, after puparium formation; ATG, autophagy-related; DIOM, dorsal internal oblique muscle; GO, gene ontology; LBWM, larval body wall muscle; LIR, LC3/Atg8-interacting regions; MER, minimal essential region; Mito-QC, mitophagy quality control; PCA, principal component analysis; TEM, transmission electron microscopy; TORC1, target of rapamycin complex 1; 3IL, third instar larvae.

Abstract

Differentiated muscle cells contain myofibrils and well-organized organelles, enabling powerful contractions. Muscle cell reorganization occurs in response to various physiological stimuli; however, the mechanisms behind this remodeling remain enigmatic due to the lack of a genetically trackable system. Previously, we reported that a subset of larval muscle cells is remodeled into adult abdominal muscle through an autophagy-dependent mechanism in *Drosophila*. To unveil the underlying mechanisms of this remodeling, we performed a comparative time-course RNA-seq analysis of isolated muscle cells with or without autophagy. It revealed both transcriptional dynamics independent of autophagy and highlighted the significance of BNIP3-mediated mitophagy in muscle remodeling. Mechanistically, we found that BNIP3 recruits autophagic machinery to mitochondria through its LC3-interacting (LIR) motif and minimal essential region (MER), which interact with Atg8a and Atg18a, respectively. Loss of BNIP3 leads to a substantial accumulation of larval mitochondria, ultimately impairing muscle remodeling. In summary, this study demonstrates that BNIP3-dependent mitophagy is critical for orchestrating the dynamic process of muscle remodeling.

Introduction

Differentiated muscle cells are intricate assemblies of myofibrils and well-organized organelles, such as T-tubules and the sarcoplasmic reticulum. Coordinated sliding of actin and myosin filaments is regulated by the dynamics of calcium ions (Ca^{2+}) released from the sarcoplasmic reticulum, while mitochondria provide ATP as the energy source driving this process. Consequently, the structural alignment of organelles and myofibrils within muscle cells is essential for the precise orchestration of contraction (Kawaguchi and Fujita, 2024). Muscle cells are long-lived and continuously undergo atrophy and hypertrophy cycles in response to growth factors, mechanical loading, nutrient status, and aging (Sartori et al., 2021). Muscle organelles also undergo remodeling as the amount of myofibrils changes, a process mediated by the ubiquitin-proteasome system. However, the mechanisms behind these processes are still poorly understood due to the lack of a genetically trackable system for analyzing muscle remodeling.

Macroautophagy, hereafter referred to as autophagy, is essential for muscle function in both flies and mammals. Autophagy is an intracellular degradation system that delivers cytosolic materials to the lysosome (Morishita and Mizushima, 2019; Nakatogawa, 2020). A flat membrane sac elongates and encloses cytosolic content to form an autophagosome, a double membrane structure. The completed autophagosome fuse with lysosomes to degrade the enclosed cargo. To date, over 40 *ATG* genes have been identified as key regulators of autophagosome formation and cargo selectivity (Nakatogawa, 2020). In mammalian muscles, the loss of autophagy leads to reduced contractile function and abnormalities in myofibrils and organelles, including mitochondria and sarcoplasmic reticulum (Karsli-Uzunbas et al., 2014; Masiero et al., 2009; Yoshii et al., 2016). We have previously reported that a subset of larval body wall muscle cells is remodeled into adult dorsal internal oblique muscles (DIOM), which functions in eclosion, through an autophagy-mediated mechanism (Fujita et al., 2017; Murakawa et al., 2020). To our knowledge, DIOM remodeling is the sole example of developmentally regulated muscle remodeling, making it an ideal model for studying muscle remodeling in general. Autophagy blockade results in severe phenotypes in DIOM (Fujita et al., 2017; Murakawa et al., 2020), yet the mechanisms by which autophagy loss induces defects remain unclear. Given that autophagy contributes to nutrient supply and transcriptional regulation (Morishita and Mizushima, 2019; Sánchez-Martín et al., 2019), it is plausible that dysfunction in autophagy could also impact gene expression during DIOM remodeling.

Autophagy can selectively target various substrates, including protein aggregates, invading bacteria into the cytosol, and organelles (Lamark and Johansen, 2021; Vargas et al., 2023). This selectivity is achieved through soluble and transmembrane cargo receptors, which bridge the cargo and autophagy machinery. Most soluble cargo receptors target ubiquitinated cargoes and harbor oligomerization domains, ubiquitin-binding domains, and LC3/Atg8-interacting regions (LIR), which is a four-residue motif [W/F/Y] -X-X-[L/V/I] (Johansen and Lamark, 2020). In contrast, transmembrane cargo receptors are anchored to target organelles and recruit autophagy machinery. Soluble and transmembrane cargo receptors confer selectivity through direct interaction with the ATG machinery. In most cases, in addition to the affinity with Atg8/LC3 via the LIR motif, interaction with core machinery components, such as ULK1, FIP200/Atg11, and Atg9, is required (Lamark and Johansen, 2021).

Mitophagy, selective autophagy for mitochondria, is physiologically crucial because mitochondrial malfunction is harmful, resulting in energy insufficiency or excess reactive oxygen species (ROS) in cells (Ney, 2015). In addition to damaged mitochondria, functional mitochondria can be removed by mitophagy to meet distinct cellular demands. Multiple mechanisms exist for mitophagy, including both soluble and transmembrane receptor-mediated mechanisms (Onishi et al., 2021). In soluble receptor-mediated mitophagy, the PINK1/Parkin axis labels mitochondria with ubiquitin. The ubiquitinated mitochondria are then recognized by NDP52 and Optineurin, soluble cargo receptors, leading to their sequestration by autophagic membranes (Narendra and Youle, 2024). On the other hand, transmembrane cargo receptors are anchored to the outer mitochondrial membrane and recruit autophagy machinery via LIR and other motifs interacting with the ATG machinery (Onishi et al., 2021). The concept of receptor-mediated mitophagy was first established in yeast ATG32 studies (Kanki et al., 2009; Okamoto et al., 2009), and then subsequently it was found that the basic mechanisms are also conserved in multicellular organisms. The list of mitochondrial outer membrane-embedded cargo receptors is growing: NIX/BNIP3L, BNIP3, FKBP8, FUNDC1, and BCL2L13 (Onishi et al., 2021). Nevertheless, their relative contribution and molecular mechanisms still need to be fully elucidated, especially under physiological conditions. So far, most mitophagy studies have been performed in cultured cells with uncouplers, hypoxia, or genetic perturbations (Yamashita et al., 2024).

NIX (also known as BNIP3L) and BNIP3 are homologous receptors for mitophagy in mammals. NIX was initially discovered as a mitophagy receptor during reticulocyte maturation. Seminal studies discovered that NIX is required to clear mitochondria from reticulocytes during differentiation (Sandoval et al., 2008; Schweers et al., 2007). Following this, its paralog BNIP3 was also shown to regulate mitophagy. NIX and BNIP3 have an LIR motif near their N-terminus and a transmembrane domain (TMD) for localization to the mitochondrial outer membrane near their C-terminus. Thereby, it has been proposed that NIX and BINP3 tether the Atg8/LC3-positive isolation membrane and mitochondria for mitophagy through these domains (Li et al., 2022; Onishi et al., 2021; Schwarten et al., 2009). In addition, Prof. Ney's group in the US identified a minimal essential region (MER), a short motif in NIX required for mitochondria clearance in reticulocytes (Zhang et al., 2012). Recently, it has been reported that the MER directly interacts with WIPIs, mammalian Atg18 orthologs, to recruit core autophagy machinery in cultured cells overexpressing BNIP3 (Adriaenssens et al., 2024; Bunker et al., 2023). Despite these findings, the roles of LIR-Atg8 and MER-Atg18 interactions in BNIP3-mediated mitophagy have not been investigated under physiological conditions.

Drosophila BNIP3, the sole ortholog of NIX and BNIP3, contains LIR, MER, and TMD, similar to its mammalian counterparts. In *Drosophila*, it has been reported that BNIP3 plays a role in programmed germline mitophagy required for mitochondrial DNA quality control (Lieber et al., 2019; Palozzi et al., 2022). However, the mechanism is not well understood. In addition, the contribution of BNIP3 to mitophagy in other physiological contexts, such as cellular differentiation or remodeling programs, has not been explored yet. In this study, we performed a comparative time-course RNA-seq analysis of isolated muscle cells, and identified BNIP3-mediated mitophagy as a critical factor in developmentally programmed muscle remodeling. We also explored the underlying mechanism by which BNIP3 tethers mitochondria with the autophagic machinery, as well as the physiological significance of BNIP3-mediated mitophagy *in vivo*.

Results

Transcriptional dynamics of DIOM remodeling during metamorphosis

During DIOM remodeling, autophagy occurs during atrophy, which lasts from 12 h to 2 d APF (after puparium formation). Then, organelle and myofibril reformation accompanies hypertrophy from 2 to 4 d APF (Fig. 1A). We previously reported the dynamics of several organelles in DIOM remodeling (Fujita et al., 2017; Murakawa et al., 2020); however, the overall mechanism is still enigmatic. To gain molecular insights into DIOM remodeling, we performed time-course RNA-seq of isolated DIOMs from four animals at five time points (Fig. 1A). Dissected animals were fixed with methanol to avoid cell death induction (Wang et al., 2021), and six DIOMs were isolated from each animal to prep total RNA (Fig. 1B). The mRNAs were amplified, and the cDNA libraries were prepared using CEL-Seq2, a sensitive protocol for single-cell RNA-seq (Hashimshony et al., 2016). Then, they are subjected to next-generation sequencing. As a result, ~8,000 genes were counted in the DIOMs above background (Supplementary file 1, ctrl). High similarities among four replicates at each time point show the reproducibility of our protocol (Fig. 1-figure supplement 1A). We performed DESeq2 principal component analysis (PCA) of all samples to reduce the dimensionality of the data (Fig. 1C and Fig. 1-figure supplement 1B). In the PC1-PC2 plane, which explains 43% of expressed genes in DIOMs, the transcriptome changed dynamically from 3IL to 4 d APF (Fig. 1C). Of note, there was a substantial difference between before (3IL) and after (4 d APF) remodeling in both PC1-2 and PC3-4 (Fig. 1C), suggesting the functional importance of remodeling larval muscle to adult abdominal muscle during this epoch.

To identify genes with similar temporal expression profiles, we used Fuzzy c-means to categorize normalized read counts into twelve clusters (Fig. 1-figure supplement 1C), each with 379 to 937 genes (Fig. 1-figure supplement 1D). The twelve clusters represent unique temporal expression dynamics, with each time point showing a distinct profile of clusters with high expression (Fig. 1D and Fig. 1-figure supplement 1D). We also noticed that a time-dependent shift in gene ontology (GO) terms is apparent among the clusters, reflecting the sequential events during DIOM remodeling (Fig. 1F). The principal component coefficients (loadings) of individual clusters to PC1 through 4 are shown in Fig. 1E. The direction and length of the arrows indicate the contribution of each cluster to principal components (PC1 to 4). Briefly, upon induction of muscle atrophy (1-2 d APF), the ubiquitin-proteasome system, developmental

signaling, autophagy, and histone modifications-related genes were upregulated. Then, chromatin remodeling-related genes were elevated around 2 d APF. Myofibril, mitochondrion, and ribosome biogenesis-related genes required for muscle hypertrophy were upregulated around 3 d APF (Fig. 1F). The data illustrates the sequential events involved in DIOM remodeling, aligning with previously observed morphological changes (Fujita et al., 2017; Murakawa et al., 2020).

Transcriptional dynamics occur independently of autophagy during DIOM remodeling

Autophagy deficiency impacts both atrophy and myofibril regeneration during hypertrophy (Fujita et al., 2017; Murakawa et al., 2020) (Fig. 2A). Given that autophagy is known to influence gene expression through both direct and indirect mechanisms (Morishita and Mizushima, 2019; Sánchez-Martín et al., 2019), we hypothesized that the loss of autophagy also alters gene expression in DIOMs. To investigate this possibility, we performed a comparative time-course RNA-seq of DIOM remodeling in *Atg18a* RNAi, *FIP200* RNAi, or *Stx17* RNAi DIOMs and compared the results with control data (Fig. 2B). Atg18a and FIP200 are essential factors for autophagosome formation, and Stx17 is an autophagosomal SNARE protein required for autophagosome-lysosome fusion (Lőrincz and Juhász, 2020; Nakatogawa, 2020). Thus, their knockdown blocks autophagy at early or late stages, respectively (Fig. 2B, bottom). Similar to the experiment in Fig. 1, we performed RNA-seq at five time points from 3IL to 4 d APF (Fig. 2B) and confirmed high similarities among the four replicates in all 20 conditions (Fig. 2-figure supplement 1A and Supplementary file 1). We confirmed that RNAi efficiently knocked down targeted genes (Fig. 2-figure supplement 1B-D). In contrast to our prediction, the knockdown of *Atg18a*, *FIP200*, or *Stx17* only had a slight impact on transcriptomic dynamics in DIOM remodeling (Fig. 2C), with only minor changes detected (Fig. 2-figure supplement 2G).

Next, to examine whether loss of autophagy affects protein synthesis in DIOMs, we used the quantification of DIOM volume changes as a surrogate measurement, and compared controls with *FIP200* RNAi from 3IL to 4 d APF (Fig. 2D and E). As expected, muscle atrophy observed until 2 d APF was affected by *FIP200* RNAi (Fig. 2A). Notably, DIOMs in the *FIP200* RNAi condition grew from 2 to 3 d APF at levels comparable to the control, indicating that protein synthesis occurs independently of autophagy. Consistent with this observation, transcription of both ribosomal RNAs and proteins, established indicators of the target of

rapamycin complex 1 (TORC1) activity (Saxton and Sabatini, 2017), did not drop but instead were slightly elevated in conditions lacking autophagy (Fig. 2-figure supplement 2). The synthesis of rRNA was upregulated in *ATG* RNAi between 2 to 3 d APF (Fig. 2-figure supplement 2A). It was confirmed that the number of nuclei remained unchanged by the loss of autophagy (Fig. 2-figure supplement 2B-C). The size of the nucleolus, which positively correlates with TORC1 activity (Grewal et al., 2007), was increased by *FIP200* and *Stx17* RNAi (Fig. 2-figure supplement 2D-F). Moreover, most ribosomal protein large subunit (RpLs) and ribosomal protein small subunit (RpSs) mRNA levels were higher in *ATG* RNAi conditions (Fig. 2-figure supplement 2G). These results suggest that TORC1 activity and protein synthesis capacity are comparable between control and autophagy-deficient DIOMs. Altogether, we conclude that gene expression occurs independently of autophagy in DIOMs.

Loss of BNIP3 leads to an accumulation of mitochondria in DIOMs

The above results suggest that the autophagic degradation of cytosolic components in itself is critical for DIOM remodeling. We have previously reported that *FIP200* RNAi or *Stx17* RNAi induce the accumulation of mitochondria or mitophagosomes, respectively (Fujita et al., 2017) (Fig. 3A and B). In addition, mitophagosomes were often observed in wild-type DIOMs at 1 d APF, when autophagy is strongly induced (Fujita et al., 2017) (Fig. 3C). These results suggest that mitochondria are major autophagy cargo, and impaired mitophagy contributes to the severe loss of autophagy phenotype.

We tried to identify relevant mitophagy receptors directly via our RNA-seq approach. The time course RNA-seq data (Fig. 1 and 2) indicated that *BNIP3* was robustly expressed in 1 d APF DIOMs among known mitophagy regulators (Fig. 3D). BNIP3 is the sole fly ortholog of mammalian NIX and BNIP3. *BNIP3* mRNA levels were relatively high at 3IL and 4 d APF when mitophagy was minimally induced. We noticed that *FBXL4* is expressed in 3IL and 4 d APF but not in 1 d APF DIOM (Fig. 3E). BNIP3 is known to undergo ubiquitination and degradation through a mechanism mediated by FBXL4, a ubiquitin E3 ligase (Niemi and Friedman, 2024). Previous data suggest that transcriptional and post-translational mechanisms regulate BNIP3 protein levels. Consistent with expression levels, *BNIP3* RNAi led to mitochondrial accumulation in 4 d APF DIOMs, whereas RNAi targeting other known mitophagy regulators did not (Fig. 3-figure supplement 1). We generated *BNIP3* knockout (KO)

flies using two gRNA to characterize BNIP3 further (Fig. 3F). *BNIP3* KO, which lacks all exons, was viable and fertile. Similar to RNAi, mitochondria accumulated significantly in *BNIP3* KO DIOMs at 4 d APF (Fig. 3G).

At the ultrastructural level, *BNIP3* KO induced the accumulation of mitochondria and loss of myofibrils (Fig. 4A and B), consistent with our confocal data (Fig. 3G). To test the role of BNIP3 in mitophagosome formation more directly, we performed TEM in the absence of Stx17 to block the autophagosome-lysosome fusion. As expected, mitophagosomes (pink-colored) were frequently observed in the *Stx17* RNAi condition (Fig. 4C and C'). In stark contrast, mitophagosomes were rare, and naked mitochondria (green-colored) accumulated in the combined condition of *Stx17* RNAi and *BNIP3* KO (Fig. 4D, D', and E). We also confirmed there was no significant difference in the number of autophagosomes (blue-colored) between the two conditions (Fig. 4F), indicating that BNIP3 is dispensable for autophagosome formation. These data show that BNIP3 is critical for mitophagosome formation in DIOMs.

The LIR and MER motifs in BNIP3 are required for the clearance of mitochondria in DIOMs

Drosophila BNIP3 harbors LIR, MER, and TMD domains, similar to mammalian NIX and BNIP3 (Fig. 5A). Although the function of the MER domain has been unknown since it was identified (Zhang et al., 2012), recent studies have shown that the MER of mammalian NIX and BNIP3 directly interacts with WIPIs, the mammalian orthologs of Atg18 (Adriaenssens et al., 2024; Bunker et al., 2023). We confirmed that this interaction is evolutionarily conserved in *Drosophila*, as HA-tagged *Drosophila* Atg18a co-immunoprecipitated with GFP-tagged Drosophila BNIP3 (Fig. 5B). Using AlphaFold 3 (Abramson et al., 2024), these two proteins are predicted to form a complex in a manner analogous to their mammalian counterparts (Fig. 5C) (Adriaenssens et al., 2024; Bunker et al., 2023). In this prediction, residues 31–57 of *Drosophila* BNIP3 (slate blue) interact with the surface formed by blades 2 (green) and 3 (pink) of the β-propeller structure of *Drosophila* Atg18a. Notably, residues 42–53 (yellow-orange), which correspond to the MER designated for NIX (Bunker et al., 2023; Zhang et al., 2012), fold into an α-helix, docking into the groove formed by blades 2 and 3 and forming substantial hydrophobic interactions as well as defined polar contacts.

Next, to verify the importance of the LIR and MER motifs in BNIP3, we expressed a series of BNIP3 mutants in *BNIP3* KO flies (Fig. 5A). ΔLIR (W16A/L19A) lacks critical consensus residues in LIR due to double mutations (Johansen and Lamark, 2020). The MER mutant (MER^{mut}, L49A) substituted residue L49 with an A, which is predicted to be deeply buried at the interface with Atg18a (Fig. 5C). The corresponding L75A mutant in human NIX has been shown to lose its affinity for WIPI2/Atg18 (Bunker et al., 2023). The ΔMER mutant lacks an entire short α-helix (G42 to Q53) of the MER motif (Fig. 5C, shown yellow-orange). The ΔLIR+ΔMER is a combined construct of ΔLIR and ΔMER. All BNIP3 constructs retain an intact TMD at the C-terminus, ensuring their localization to the outer mitochondrial membrane (Fig. 5-figure supplement 1).

As shown in Fig. 5D, the expression of the full-length (Full) construct almost completely suppressed the accumulation of mitochondria in BNIP3 KO at 4 d APF, confirming the rescue of BNIP3 function using our construct-based approach. To our surprise, the BNIP3 ΔLIR construct rescued the *BNIP3* KO phenotype comparable to Full, indicating LIR on its own may be redundant for mitophagy in DIOMs. In contrast, mitochondria accumulated in MER^{mut} and ΔMER reconstituted DIOMs. Furthermore, the combination of ΔLIR and ΔMER resulted in mitochondria accumulation nearly identical to that observed in BNIP3 KO flies (Fig. 5D and D'). Consistent with these findings, *Atg101*-dependent autophagic degradation of GFP-BNIP3 was strongly suppressed by the ΔLIR+ΔMER mutations (Fig. 5E). Atg101 is an essential subunit of the Atg1/ULK1 kinase complex (Guo et al., 2019; Hegedus et al., 2014; Noda and Mizushima, 2016). From these results, we conclude that both MER and LIR motifs contribute to BNIP3-mediated mitophagy, with some redundancy in their contributions to selectivity.

BNIP3-mediated mitophagy eliminates larval muscle mitochondria during muscle remodeling

The data above suggest that a BNIP3-mediated mechanism degrades larval muscle-derived mitochondria; however, in previous figures, we only observed the terminal phenotype of *BNIP3* KO at 4 d APF. To observe the changes in the number of mitochondria during DIOM remodeling, we first performed a time-course experiment of Mito-GFP in control or *BNIP3* KO conditions (Fig. 6A and Fig. 6-figure supplement 1A and B). There was no significant difference in the number of mitochondria at 3IL; however, mitochondria started accumulating at

1 d APF (Fig. 6A and A'), suggesting that BNIP3-mediated mitophagy degrades larval muscle mitochondria. Further, we tested the Mito-QC probe (Lee et al., 2018), a tandem GFP-mCherry fusion protein targeted to the OMM, to compare mitophagy flux at 1d APF with and without BNIP3. When the probe is delivered to lysosomes via autophagy, the GFP is quenched due to the acidic environment of the lysosome. Robust mitophagy activity was detected in control DIOMs at 1 d APF (Fig. 6B left). In sharp contrast, *BNIP3* KO blocked mitophagy flux at a comparable level with *FIP200* RNAi (Fig. 8B middle and right).

To show the degradation of larval muscle-derived mitochondria more directly, we labeled larval muscle mitochondria specifically by using the temperature-sensitive mutant of GAL80 ($GAL80^{ts}$), a repressor of GAL4 (Mcguire et al., 2004). At the restrictive temperature (29˚C), the $GAL80^{ts}$ mutant is inactive, allowing GAL4 to drive the expression of the UAS-fused construct, UAS-Mito-GFP. Conversely, at the permissive temperature (18˚C), the $GAL80^{ts}$ is active, suppressing GAL4 activity. Using this system, Mito-GFP was expressed in the larval muscle and subsequently suppressed throughout the entire pupal stage (Fig. 6C). Anti-ATP5A antibodies were used to visualize total mitochondria. The amount of Mito-GFP-positive mitochondria was comparable in control and *BNIP3* KO at 3IL muscle. However, at 4 d APF, the Mito-GFP signal was nearly absent in the control, while a strong Mito-GFP signal was observed in the *BNIP3* KO (Fig. 6D and D'), indicating that BNIP3-mediated mitophagy degrades larval muscle mitochondria during muscle remodeling.

Discussion

The transcriptional dynamics associated with DIOM remodeling is largely independent of autophagy (Fig.2). Instead, our RNA-seq data suggest that it is regulated primarily by ecdysone signaling, with minimal influence from autophagy inhibition. However, a subset of genes exhibited altered expression levels in autophagy-deficient conditions (Fig. 2-figure supplement 2G). Of note, their expression levels were consistently upregulated or downregulated throughout all time points. Since no apparent phenotype was observed in *ATG* knockdown 3IL body wall muscles (Fujita et al., 2017), the observed expression changes are unlikely to underlie the loss-of-autophagy phenotype in DIOM remodeling. Furthermore, *FIP200* RNAi had minimal impact on the DIOM growth rate (Fig. 2 D and E), which reflects translational capacity. From these data, we conclude that the contribution of autophagy to gene expression during DIOM remodeling is minimal.

In the RNA-seq experiments (Fig. 2), *ATG* genes were exclusively depleted in muscle cells; thus, autophagy in non-muscle organs remained intact. It is plausible that essential nutrients for DIOM hypertrophy, such as amino acids, were supplied by other organs, including the fat body (Murakawa et al., 2022). Alternatively, the necessary amino acids might have been derived from myofibril breakdown via the ubiquitin-proteasome system (Quy et al., 2013).

Transcriptome changes before and after DIOM remodeling reflect adaptations to the shift from the anaerobic environment of larvae to the aerobic environment of adults, alongside alterations in nutritional pathways. Notable changes in energy production systems occurred between the 3IL stage (pre-remodeling) and 4 d APF (post-remodeling) (Fig. 1). Glycolysis-associated genes exhibited high expression levels at the 3IL stage, followed by a significant decline during the pupal and adult stages. For instance, the expression of *Lactate dehydrogenase* (*Ldh*), a key enzyme in switching between anaerobic and aerobic respiration (Liang et al., 2023; Semenza, 2014), was particularly noteworthy. Ldh catalyzes the conversion of pyruvate to lactate while regenerating NAD^+ from NADH under anaerobic conditions. Ldh levels were markedly high in larval muscles, suggesting reliance on anaerobic glycolysis. Conversely, its reduced expression in remodeled adult muscles reflects a metabolic shift toward aerobic pathways.

Genes related to serine-centered amino acid and lipid catabolism, both of which rely on oxygen to produce ATP, were significantly upregulated in adult muscles. For example, the

expression of *Alanine-glyoxylate aminotransferase* (*Agxt*), an enzyme that converts alanine to pyruvate, was approximately 100 times higher in adult muscles compared to larvae. Similarly, *brummer* (*bmm*), a triacylglycerol lipase, exhibited a fivefold increase, suggesting enhanced reliance on fatty acids metabolized via β-oxidation and the TCA cycle. These findings highlight the shift in energy sources from glycolysis in larval muscles to amino acids and lipids in adult muscles, metabolized aerobically in mitochondria.

A recent study suggests that DIOMs are a primary source of pupal ecdysone (Zhang et al., 2024). In line with this data, our time-course mRNA-seq analysis revealed high expression of *Phm*, an enzyme essential for ecdysteroid biosynthesis, at 1 d APF (supplemental file 1). However, other Halloween genes required for ecdysteroid biosynthesis, such as *Nvd*, *Spo*, *Spok*, *Dib*, *Sad*, and *Shd* (Kamiyama and Niwa, 2022), were not, or only minimally, expressed in DIOMs during metamorphosis (supplemental file 1). Consequently, whether DIOMs directly secrete ecdysone remains unclear. Instead, DIOMs may contribute to a specific step in the ecdysteroid biosynthesis pathway, potentially supplying intermediate 5β-ketotriol to other tissues for further conversion.

Functional mitochondria are degraded during developmental muscle remodeling; therefore, it is reasonable that a membrane-anchored mitophagy receptor, directly interacting with the autophagic machinery, is selected over a ubiquitination-mediated mechanism involving PINK1 and Parkin. The PINK1/Parkin axis is activated by mitochondrial membrane potential depolarization (Narendra and Youle, 2024), which is not observed in remodeling muscles. The protein level of BNIP3 appears to be regulated at transcriptional and post-translational levels (Fig. 3E). It is known that BNIP3 is degraded via a mechanism mediated by Fbxl4, a ubiquitin E3 ligase (Niemi and Friedman, 2024). The balance between synthesis and degradation likely results in the highest BNIP3 protein levels at 1 d APF, a time when mitophagy is robustly induced. However, BNIP3 protein levels have not been directly confirmed, as isolating a sufficient number of DIOMs for western blotting is challenging. Generating a GFP knock-in line for BNIP3 would allow for an imaging-based assay to measure its protein levels during DIOM remodeling.

Overexpression of BNIP3 in larval muscle cells did not significantly induce mitophagy (data not shown), suggesting that BNIP3 expression alone is insufficient to drive mitophagy. BNIP3-mediated mitophagy likely requires not only BNIP3 expression but also autophagy

induction. We propose that autophagy induction in DIOMs at the early pupal stage is regulated by ecdysone signaling, similar to other instances of developmental autophagy in *Drosophila* (Murakawa et al., 2022). Understanding the mechanisms by which developmental signals trigger autophagy remains a critical question for future research.

A key function of autophagy in DIOM remodeling is the degradation of mitochondria from larval muscles. In the absence of BNIP3, mitochondria derived from the larval muscle accumulate and physically obstruct myofibril formation during hypertrophy (Fig. 6E). Myofibrils typically form beneath the sarcolemma (Mao et al., 2022; Sanger et al., 2010); therefore, when mitochondria accumulate, myofibrils are restricted to the cell periphery. Interestingly, unlike *ATG* RNAi, *BNIP3* knockout muscles exhibited relatively normal but thinner myofibrils (Fig. 3G). In contrast, *ATG* RNAi not only caused mitochondrial accumulation but also severely disrupted myofibril organization, as indicated by misaligned sarcomeres (Fujita et al., 2017; Murakawa et al., 2020). These findings suggest that autophagy contributes to DIOM remodeling beyond mitochondrial degradation. Schnorrer's group in France has demonstrated that mechanical tension is essential for sarcomere assembly and maturation (Mao et al., 2022; X. Zhang et al., 2024). Given that *ATG* RNAi disrupts DIOM attachment (Murakawa et al., 2020; Ribeiro et al., 2011), it is possible that reduced tension—caused by an unknown mechanism—leads to disorganization of myofibrils in DIOMs when autophagy is impaired.

Contrary to the previous model, the LIR motif of BNIP3 was found to be dispensable for mitophagy in DIOMs (Fig. 5D and E). Our findings align with reports stating that the clearance of mitochondria in reticulocytes is independent of the LIR motif (Novak et al., 2010; Zhang et al., 2012). Together, this suggests that the dependency on the LIR motif may differ between *in vitro* and *in vivo* contexts. In studies of BNIP3 in cultured cells, such as HeLa cells, BNIP3 is often overexpressed, and mitophagy is induced through chemical treatments (Bunker et al., 2023; Yamashita et al., 2024). These experimental conditions may account for the observed differences in LIR dependency. Understanding the factors that drive these contextual variations in BNIP3-mediated mitophagy will require further investigation.

The MER motif in BNIP3 is required for mitophagy in *Drosophila*. Similar to its mammalian counterpart, the MER motif of *Drosophila* BNIP3 is predicted to interact with the groove between blades 2 and 3 of the β-propeller in Atg18a (Fig. 5C). Notably, this groove of

Atg18 overlaps with the binding site for Atg16 (Strong et al., 2021). We propose that the BNIP3 MER-Atg18a interaction functions at the early stages of mitophagosome formation, which is later replaced by the Atg16-Atg18a interaction during the elongation phase. In this sequential model, the BNIP3 LIR-Atg8a interaction would dominate at the elongation steps. Alternatively, the MER-Atg18a and LIR-Atg8a interactions might serve redundant roles in determining selectivity, as both Atg8 and Atg18 localize to the elongating autophagic membranes. This redundancy could explain why the LIR motif is dispensable for BNIP3-mediated mitophagy (Fig. 5D and E).

Martens's group (Austria) recently reported that WIPIs, the mammalian orthologs of Atg18, bind to Atg13, a component of the FIP200/ULK1 complex (Adriaenssens et al., 2024). They propose that the NIX/BNIP3-WIPI-Atg13 axis induces selective autophagy for mitochondria, analogous to known selective autophagy receptors associated with FIP200 (Lamark and Johansen, 2021). It would be interesting to test whether an artificial interaction motif with the Atg1 complex could compensate for the loss of function of ΔMER in DIOMs.

Our study provides new insights into the mechanisms underlying autophagy-associated muscle remodeling. Transcriptional dynamics uncovered a sequence of events involving muscle atrophy and hypertrophy, offering a valuable dataset for understanding the process of muscle remodeling. In addition, we provided insights into the mechanism and significance of BNIP3-mediated mitophagy *in vivo*. These findings are particularly important given the evolutionary conservation of muscle remodeling mechanisms between *Drosophila* and mammals (Piccirillo et al., 2014). Future studies should explore the broader implications of our findings across various cellular, developmental, and organismal contexts.

Materials and methods

Reagents and antibodies

The following antibodies were used: Mouse monoclonal anti-ATP5A (1:300, ab14748, Abcam, Cambridge, UK), Rat monoclonal anti-HA (1:1000; 11867423001, Roche, Basel, Switzerland), Rabbit polyclonal anti-GFP (1:2000; 598, MBL, Nagoya, Japan), Rabbit polyclonal anti-Fibrillarin (1:300; ab5821, Abcam, Cambridge, UK), anti-rabbit IgG Alexa Fluor 594 conjugate (1:400; A11012, Thermo Fisher Scientific, Waltham, USA), anti-mouse IgG Alexa Fluor 488 conjugate (1:400; A11001, Thermo Fisher Scientific, Waltham, USA), anti-mouse IgG Alexa Fluor 594 conjugate (1:400; A11005, Thermo Fisher Scientific, Waltham, USA), HRP-conjugated AffiniPure Goat Anti-Rabbit IgG (1:10000; 111-035-144, Jackson ImmunoResearch, West Grobe, USA), HRP-conjugated AffiniPure Donkey Anti-Rat IgG (1:5000; 712-005-153, Jackson ImmunoResearch, West Grobe, USA), Bisbenzimide H33342 Fluorochrome Trihydrochloride DMSO Solution (1:10000; 04915-81, Nacalai Tesque, Kyoto, Japan), Alexa Fluor 633 Phalloidin (1:200; A22284, Thermo Fisher Scientific, Waltham, USA), and GFP-Trap Agarose (gta, Chromotek, Planegg-Martinsried, Germany).

Drosophila strains

Flies were reared under standard conditions at 25˚C unless otherwise stated. The w^{1118} strain was used as a control for knockout strains. For muscle-targeted gene expression, Mef2-GAL4 was used. UAS-*LacZ* was used as a control for UAS transgenes. All genetic combinations were generated by standard crosses. Detailed genotypes are described in Supplemental table 1. Genotypes of flies used in this study include the following: (1) y^{1} *w**; *P*{w^{+mC}=*GAL4-Mef2.R*}3 (Bloomington *Drosophila* Stock Center, BL 27390; DMef2-GAL4), (2) w^{1118}; *P*{w^{+mC}=*UAS-lacZ.B*}*Bg4-1-2* (BL 1776; UAS-LacZ), (3) w^{*}; *P*{w^{+mC}=*UAS-Rheb.Pa*}*2* (BL 9688), (4) w^{1118}; *P*{w^{+mC}=*UAS-mito-HA-GFP.AP*}*2/CyO* (BL 8442; Mito-GFP), (5) w^{1118}; *P*{$y^{+t7.7}$ w^{+mC}=*UAS-mito-QC*}*attP16* (BL 91640, Mito-QC), (6) w^{1118}; *P*{w^{+mC}=*UAS-Dcr-2.D*}*10* (BL 24651, *UAS-Dcr2*), (7) y^{*} w^{*}; *P*{w^{+mC}=*UAS-tdTomato.mito*}*2* (Kyoto DGGR 117016, tdTomato-Mito), (8) *w*; *UAS-IR-Atg18a*^{KK100064} (VDRC 105366; Atg18a RNAi), (9) *w*; *UAS-IR-Stx17*^{KK100034} (VDRC 108825; Stx17 RNAi), (10) *w*; *UAS-IR-BNIP3*^{KK111246} (VDRC 107493; BNIP3 RNAi), (11) *w*; *UAS-IR-Pink1*^{KK101205} (VDRC 109614; Pink1 RNAi), (12) *w*; *UAS-IR-Park*^{KK107919} (VDRC 104363; Park RNAi), (13) *w*; *UAS-IR-CG12511*^{KK109618} (VDRC

101785; CG12511 RNAi), (14) *w*; *UAS-IR-Zonda*^{KK107775} (VDRC 110620; Zonda RNAi), (15) y^1 sc^* v^1 sev^{21}; *P*{$y^{+t7.7}$ $v^{+t1.8}$=*TRiP.HMS01611*}*attP2*/*TM3, Sb*^{1} (TRiP, BL 36918; FIP200 RNAi), (16) y^1 v^1; *P*{$y^{+t7.7}$ $v^{+t1.8}$=*TRiP.JF01937*}*attP2* (TRiP, BL 25896; Stx17 RNAi), (17) y^1 sc^* v^1 sev^{21}; *P*{$y^{+t7.7}$ $v^{+t1.8}$=*TRiP.GL00156*}*attP2* (TRiP, BL 35578; mTor RNAi), (18) *w*; *UAS-tub-GAL80*^{ts} (from E. Kuranaga), (19) *w*; *UAS-mCD8:GFP*, (20) *w; DMef2-GAL4*, *UAS-Dcr2* (Fujita et al., 2017), (21) *w*; *UAS-Dcr2*; *DMef2-GAL4*, *sqh-YFP:Mito*^{BL7194}/*TM6C Sb Tb* (Murakawa et al., 2020). New genotypes generated during this study include the following: (22) *w**;; *BNIP3 KO CRISPR{3xP3-RFP}/TM6B*, *Tb*^{1}, (23) w^{1118}, *Atg101 KO CRISPR{3xP3-RFP}/FM7a* (24) w^{1118}; *UASt-GFP-BNIP3_full*^{attP40}, (25) w^{1118}; *UASt-GFP-BNIP3_ΔLIR* (*W16A/L19A*)^{attP40}, (26) w^{1118}; *UASt-GFP-BNIP3_MER mutant* (*L49A*)^{attP40}, (27) w^{1118}; *UASt-GFP-BNIP3_ΔMER* (*Δ*42-53)^{attP40} and (28) w^{1118}; *UASt-GFP-BNIP3_ ΔLIR+ΔMER*^{attP40}.

DNA engineering

Plasmid vectors were constructed using standard molecular biology techniques. The DNA polymerase KOD One (TOYOBO, Osaka, Japan) and PrimeSTAR GXL Premix (Takara Bio, Shiga, Japan) were used for PCR amplification. The DNA fragments were assembled using the Gibson Assembly. Construction of the expression vectors of GFP-tagged BNIP3_full under UAS control (pUASt-attB-GFP-BNIP3) was as follows: *Drosophila* BNIP3 CDS was amplified from template RE48077 (DGRC Stock 9148; https://dgrc.bio.indiana.edu//stock/9148 ; RRID:DGRC_9148) using the following primer sets: 5'-ATGTCTACGACACCAAAATCGAG-3' and 5'-TCAGTCAATGACCACACGG-3'. This fragment of BNIP3 CDS was ligated into the linearized pUAST-attB-GFP vector, which is amplified with the following primer sets: 5'-CGTGTGGTCATTGACTGAGCGGCCGCGGCTCGAGGGTACC-3' and 5'-TTGGTGTCGTAGACATGGTGAAGGGGGCGGCCGCGGAG-3'. To generate plasmids with mutations or deletions in the BNIP3 coding sequence (pUAST-attB-BNIP3_ΔLIR, pUAST-attB-BNIP3_MER$^{mut\ (L49A)}$, and pUAST-attB-BNIP3_ΔMER), the plasmid pUAST-attB-GFP-BNIP3_full was used as a template. For the construction of pUAST-attB-BNIP3_ΔLIR, these primer sets: 5'- CTGCGATCGAAGCGAGCACAACAGCTGCGATG-3' and 5'-CTCGCTTCGATCGCAGATTCGCCCAGCAAATC-3' were used to introduce the W16A/L19A mutations. For the construction of pUAST-attB-BNIP3 MER$^{mut\ (L49A)}$, these primer

sets: 5'-AGACTTGCGCGCGAGGCCCAGCGCGAG-3' and 5'-CTCGCGCGCAAGTCTCAGGTACTCCTC-3' were used to introduce the L49A mutation. For the construction of pUAST-attB-BNIP3_ΔMER, these primer sets: 5'-CAACAATCGCGAGTCGAACCAGTCG-3' and 5'-GACTCGCGATTGTTGAATGGCAACGG-3' were used to delete G42 to Q53. To generate a construct that harbors both ΔLIR and ΔMER (pUAST-attB-BNIP3_ΔLIR+ΔMER), the plasmid pUAST-attB-GFP-BNIP3_ΔMER was used as a template. The same primer sets as pUAST-attB-BNIP3_ ΔLIR construction were used for amplification. Each resultant linear DNA fragment was ligated into a circular plasmid. Construction of the expression vectors of 3xHA-tagged Atg18a under UAS control (pUASt-attB-3xHA-Atg18) was as follows: *Drosophila* Atg18a CDS was amplified from template LD38705 (DGRC Stock 2722; https://dgrc.bio.indiana.edu//stock/2722 ; RRID:DGRC_2722) using the following primer sets: 5'-TTCCAGATTACGCTGGATCCATGATGAGCCTGCTCGGGC-3' and 5'-TACCCTCGAGCCGCGGCCGCTTAAGCACCTTTGATATCCATGGC-3'. The resultant fragment of Atg18a was ligated into the linearized pUAST-attB-3xHA vector, which was amplified with the following primer sets: 5'-GCGGCCGCGGCTCGAGGGTACCAGCTCTAC-3' and 5'-GGATCCAGCGTAATCTGGAACGTCATATGG-3'. All the resultant vectors were validated by DNA sequencing.

Generation of mutant and transgenic flies

To generate *Drosophila* mutants with a knockout of *BNIP3* (CG5059) or *Atg101* (CG7053), the CRISPR/Cas9 system was used, following a modified method based on Kondo and Ueda (Kondo and Ueda, 2013). Guide RNA (gRNA) sets for *BNIP3* KO and *Atg101* KO were designed as follows: for *BNIP3* KO, upstream gRNA sequences, 5'-CGTCAACACCAAAGATAACT[TGG]-3' and downstream gRNA sequences 5'-CTTTCAGTCAATGACCACAC[GGG]-3'; for *Atg101 KO*, upstream gRNA sequences 5'-GTCCACCTGACGACCCTCCA[TGG]-3' and downstream gRNA sequences 5'-CTCGCAATGTGACGGGCTGT[CGG]-3'. Each gRNA was individually cloned into a plasmid under the control of U6 promoter. A donor DNA cassette containing a 3x P3-RFP selection marker, loxP sites, and two homology arms was cloned into the pUC57-Kan plasmid for DNA

repair. The gRNAs targeting *BNIP3* or *Atg101,* and the hs-Cas9 coding DNA plasmids, along with the donor plasmid, were microinjected into embryos of the w^{1118} strain. F1 files were screened by a selection marker of 3x P3-RFP and validated by genomic PCR and sequencing (WellGenetics Inc.). To generate a series of UASt-GFP-BNIP3 transgenic flies, the vectors described above were injected into embryos for phiC31-mediated insertion (WellGenetics Inc.).

RNA-seq analysis of DIOMs

For collecting DIOMs or their precursors, larvae or pupae were dissected and fixed with methanol. Six DIOMs were isolated from each animal using forceps and a pipette under a stereomicroscope (SZX16, EVIDENT, Tokyo, Japan). The collected muscle cells were lysed with BLA buffer (ReliaPrep Tissue RNA Miniprep System, Promega) and stored at -80˚C. Following sample preparation, the frozen samples were thawed, and total RNA was extracted and eluted in RNase-free water according to the manufacturer's protocol (ReliaPrep Tissue RNA Miniprep System, Promega). Subsequently, cDNA libraries were prepared using CEL-Seq2, a single-cell RNA-seq protocol (Hashimshony et al., 2016). Briefly, reverse transcription was performed using poly(T) primers with a T7 promoter to generate single-stranded DNA from mRNA, which was then converted into double-stranded DNA through second-strand synthesis. Amplified RNA was produced via in vitro transcription using the MEGAscript T7 kit (Thermo Fisher Scientific, Waltham, MA) and subsequently reverse transcribed to construct the cDNA library. Library sequencing was performed using the NovaSeq6000. Cell barcode and UMI in Read1 were extracted by using UMI-tools with the following command "umi_tools extract -I read1.fastq —read2-in=read2.fastq --bc-pattern=NNNNNNNNNNCCCCCCCC". Adaptor sequence and low-quality sequence were removed, read lengths below 20bp were discarded by using Trim Galore, and reads were mapped to the GRCm38 reference using HISAT2. Read counts for each gene were obtained by featureCounts, and UMI duplications were removed. The expression levels of genes in each sample were determined from the UMI counts after a normalization process using the DESeq2 package in R. The R programming language was used for each type of analysis, utilizing the pheatmap package for cluster analysis, the prcomp package for principal component analysis (PCA), and the Mfuzz package for fuzzy c-means clustering analysis (Kumar and Futschik, 2007).

Quantification of rRNA in DIOMs

Total RNA was extracted as described in the "RNA-seq analysis of DIOMs" section. The quality and composition of the extracted RNA were assessed using the Agilent 2100 Bioanalyzer system with the RNA 6000 Pico Kit (Agilent, Santa Clara, USA). Ribosomal RNA (rRNA) content in the DIOMs was quantified by measuring the peak areas corresponding to 18S and 28S rRNA within the total RNA profile.

Immunofluorescence staining

Muscle preparations were performed as previously described (Ribeiro et al., 2011). 3IL or pupae were pinned on a Sylgard-covered petri dish in dissection buffer (5 mM HEPES, 128 mM NaCl, 2 mM KCl, 4 mM $MgCl_2$, 36 mM sucrose, pH 7.2). The animals were pinned flat and fixed (4% PFA, 50 mM EGTA, PBS) at room temp for 20 min. Then, the samples were unpinned and blocked (0.3% bovine serum albumin, 0.6% Triton X100, PBS) at room temp for 5 min, incubated with primary antibody overnight at room temperature, washed with PBS, and incubated with Alexa Fluor 488 or 594-conjugated secondary antibody (Thermo Fisher Scientific, Waltham, MA) for 2 h at room temperature. The immunostained samples were washed and mounted in FluorSave reagent (Merck Millipore, Darmstadt, Germany).

Confocal fluorescence microscopy

To image live pupal DIOMs, staged pupae were removed from their pupal cases and mounted between a slide glass and a cover glass following the protocol described by Zitserman and Roegiers (Zitserman and Roegiers, 2011). Imaging was performed through the dorsal cuticle. Both live and fixed samples were observed using a confocal microscope (FV3000, EVIDENT, Tokyo, Japan) equipped with either a 60× silicone/1.30 NA UPlanSApo or a 4×/0.16 objective lens (EVIDENT, Tokyo, Japan). FLUOVIEW (EVIDENT, Tokyo, Japan) was used for image acquisition, and the exported images were processed and analyzed with ImageJ (NIH, Bethesda, USA).

Transmission electron microscopy

Staged pupae (1 d or 4 d APF) were removed from pupal cases, pinned on a Sylgard-covered petri dish, and dissected directly in fixative (2% paraformaldehyde, 2.5% glutaraldehyde, 150

mM, 5 mM calcium chloride, sodium cacodylate, pH 7.4). They were then fixed for 2 h at room temperature followed by overnight at 4˚C. The dissected fillets were washed with 0.1 M phosphate buffer pH 7.4, post-fixed in 1% OsO_4 buffered with 0.1 M phosphate buffer for 2 h, dehydrated in a graded series of ethanol, and embedded flat in Epon 812 (TAAB, Aldermaston, UK). Ultrathin sections (70 nm thick) were collected on copper grids covered with Formvar (Nisshin EM, Tokyo, Japan), double-stained with uranyl acetate and lead citrate, and then observed using a JEM-1400Flash transmission electron microscope (JEOL, Tokyo, Japan).

Immunoblots and Immunoprecipitation

For immunoblots, five larval fillets were collected for each sample. The samples were lysed directly in 1.5x sample loading buffer [100 mM Tris-HCl (pH 6.8), 3% SDS, 15% glycerol, and 0.0015% Bromophenol Blue]. Equal amounts of proteins per sample were subjected to SDS-PAGE and transferred to Immobilon-PSQ PVDF transfer membrane (Merck Millipore, Darmstadt, Germany) with Trans-Blot Turbo Transfer System (Bio-Rad, Hercules, CA, USA). The membranes were blocked with TBS-T buffer [10 mM Tris-HCl (pH 8.0), 150 mM NaCl, 0.1% Tween 20, PBS] containing 5% skim milk for 1 h, and were then incubated with primary antibodies in Can Get Signal Solution 1 (TOYOBO, Osaka, Japan) overnight at 4˚C. Membranes were washed three times with TBST, incubated with HRP-conjugated secondary antibodies in the blocking buffer for 2 h at room temperature, and washed five times with TBST. Immunoreactive bands were detected using Clarity Western ECL Substrate (Bio-Rad, Hercules, CA, USA) and the ChemiDoc MP Imaging System (Bio-Rad, Hercules, CA, USA). The images were processed using ImageJ.

For immunoprecipitation, S2 cells were transfected with plasmids using jetPRIME transfection reagent (Polyplus-transfecton, Illkirch, France) according to the manufacturer's instructions. Plasmid encoding Actin-GAL4 (gift from E. Kuranaga), pUASt-attB-3xHA-Atg18, and pUASt-attB-GFP-BNIP3 were used. After 48 h transfection, cells were washed with PBS and harvested in lysis buffer [20 mM Tris-HCl (pH7.4), 1 mM EDTA, 150 mM NaCl, 1% NP-40, 1 mM PMSF, and protease inhibitor cocktail (Nacalai Tesque, Kyoto, Japan)]. Cell lysates were centrifuged at 17,000 x g for 1 min at 4˚C, and the supernatant was filtered using a 0.22 μm filter tube (Merck Millipore, Darmstadt, Germany). The filtrated lysates were incubated with GFP-Trap agarose beads (Chromotek, Planegg-Martinsried, Germany) for 2 h at 4˚C with

gentle rotation. After 2 h of incubation, beads were washed three times with Wash Buffer A [10 mM Tris-HCl (pH7.4), 0.5 mM EDTA, 150 mM NaCl, 1% Nonidet P-40 substitute], followed by twice with Wash Buffer B [10 mM Tris-HCl (pH7.4), 0.5 mM EDTA, 150 mM NaCl] to remove non-specific proteins. Bound proteins were eluted by boiling in 2x sample buffer for 5 min, and subsequent steps were performed as described above for immunoblots.

Structure prediction and visualization

The amino acid sequences of *Drosophila* BNIP3 (Q9VPD6) and Atg18a (Q9VSF0) were retrieved from the UniProt Knowledgebase (https://www.uniprot.org/uniprotkb/) and submitted to the AlphaFold Server (https://alphafoldserver.com/) to predict the structure of their complex. The PyMOL Molecular Graphics System (Version 2.5.4; Schrödinger, LLC) was then used to analyze the resulting five predictions and visualize the top-ranked structure.

Image analyses

For cell volume measurement (Fig. 2E), the DIOMs expressing GFP were imaged at 1 μm intervals. The muscle cell volume was calculated by multiplying the area of each XY slice by the interval length and summing the results across all slices. To measure nucleolus and nucleus volume (Fig. 2-figure supplement 2E and F), DIOMs stained for DNA (H33342) and Fibrillarin were imaged at 0.5 μm intervals. DAPI- and anti-Fibrillarin-stained areas were extracted by binarization using ImageJ. This process was repeated for the z-stacks, and the nucleolus and nucleus volume were determined by multiplying the area of each slice by the interval length between slices. Quantification of the number of autophagosomes, mitophagosomes, or mitochondria in TEM images was conducted as follows (Fig. 4E and F): Double-membrane-bound structures containing undigested cytoplasmic contents (autophagosomes), autophagosomes enclosing mitochondria (mitophagosomes), and naked mitochondria were manually counted. At least 17 images derived from multiple animals were analyzed for each genotype. To categorize mitochondrial accumulation in DIOMs, at least 50 DIOMs from 5 animals were analyzed for each genotype (Fig. 5D'). Samples were blinded to minimize bias before observation by a confocal microscope. DIOMs were categorized into three groups of mitochondrial accumulation (Regular, Medium, and High) based on the tdTomato-Mito channel signal. For the Mito-QC assay, a representative DIOM was imaged for each genotype and

analyzed by ImageJ (Fig. 6B). Image preprocessing included filtering and background subtraction for both GFP and mCherry channels. Dot plots were then generated, and Spearman's correlation coefficients for GFP and mCherry intensities were calculated using the *Coloc2* plugin in ImageJ. Mitochondrial accumulation was quantified as follows (Fig. 6A' and D'): At least five DIOMs per fly were examined, with three biological replicates analyzed for each genotype. Cellular regions containing F-actin were manually segmented, and GFP channel intensity within these segmented areas was measured for quantification. For Fig. 6A', image preprocessing steps, filtering, background subtraction, and intensity binarization were applied to the GFP channel using ImageJ to minimize noise. The area of each detected object was measured, and the total area was defined as the sum of mitochondrial areas. Then, the values were normalized to the cellular region area. For Fig. 6D', GFP intensity quantification was performed as follows: Since the signals in the 3IL BWM images were weaker than those in 4 d APF, the intensity of the GFP channel was uniformly enhanced at an equal scale. All images were subjected to preprocessing, including filtering and background subtraction. The mean GFP intensity within each segmented area was then measured and normalized, with the mean GFP intensity of control for each stage set to 1.

Statistics

Each experiment was performed with at least three different cohorts of unique flies analyzed. One exception was for TEM analyses, performed on two parallel replicates with multiple animals each. All experiments were performed in parallel with controls. Error bars show the standard deviation for bar charts. When more than two genotypes were used in an experiment, Sidak's test or Dunnett's T3 multiple comparisons test was used (GraphPad, Prism9 version 9.5.1). Mann-Whitney tests were used to compare two means. $P<0.05$ was regarded as statistically significant (*$P<0.05$, **$P<0.001$, ***$P<0.0001$, and ****$P<0.00001$).

Acknowledgments

We are grateful to JH. Lee (Univ. of Michigan), T. Yoshimori (Osaka Univ.), E. Kuranaga (Kyoto Univ.), BDSC, VDRC, DGRC, and NIG-fly for reagents. We thank Y. Shimada and R. Niwa (Univ. of Tsukuba) for the helpful discussion. We thank the Biomaterials Analysis Division of the Institute of Science Tokyo for the DNA sequencing. We are grateful to M. Landekic (McGill Univ.) for English editing. This work was supported in part by Grant-in-Aid for Transformative Research Areas (B) (grant number 21H05147, NF), Japan Science and Technology Agency (JST) PRESTO (grant number JPMJPR18H8, NF), AMED PRIME (grant number 24gm6410016h0001, NF), and MEXT Promotion of Development of a Joint Usage / Research System Project: Pan-Omics DDRIC, MRCI for High Depth Omics, CURE: JPMXP1323015486 for MIB and RIIT in Kyushu University.

Author contributions

NF conceived the project. HT, TM, TKanki, YO, and NF designed the experiments. HT, TM, KK, MK, TKaminishi, YS, KT, AH, and NF performed the experiments. HT, TM, and NF analyzed and interpreted data. YO contributed to the materials. NF took the lead in writing the manuscript. All authors provided critical feedback and helped shape the research and manuscript.

Competing financial interests

The authors declare no competing financial interests.

References

Abramson J, Adler J, Dunger J, Evans R, Green T, Pritzel A, Ronneberger O, Willmore L, Ballard AJ, Bambrick J, Bodenstein SW, Evans DA, Hung CC, O'Neill M, Reiman D, Tunyasuvunakool K, Wu Z, Žemgulytė A, Arvaniti E, Beattie C, Bertolli O, Bridgland A, Cherepanov A, Congreve M, Cowen-Rivers AI, Cowie A, Figurnov M, Fuchs FB, Gladman H, Jain R, Khan YA, Low CMR, Perlin K, Potapenko A, Savy P, Singh S, Stecula A, Thillaisundaram A, Tong C, Yakneen S, Zhong ED, Zielinski M, Žídek A, Bapst V, Kohli P, Jaderberg M, Hassabis D, Jumper JM. 2024. Accurate structure prediction of biomolecular interactions with AlphaFold 3. *Nature* **630**:493–500. doi:10.1038/s41586-024-07487-w

Adriaenssens E, Schaar S, Cook ASI, Stuke JFM, Sawa-Makarska J, Nguyen TN, Ren X, Schuschnig M, Romanov J, Khuu G, Lazarou M, Hummer G, Hurley JH, Martens S. 2024. Reconstitution of BNIP3/NIX-mediated autophagy reveals two pathways and hierarchical flexibility of the initiation machinery. *bioRxiv* doi:10.1101/2024.08.28.609967

Bunker EN, Le Guerroué F, Wang C, Strub M, Werner A, Tjandra N, Youle RJ. 2023. Nix interacts with WIPI2 to induce mitophagy. *EMBO J* **42**. doi:10.15252/embj.2023113491

Fujita N., Huang W, Lin T-H, Groulx J-F, Jean S, Nguyen J, Kuchitsu Y, Koyama-Honda I, Mizushima N, Fukuda M, Kiger AA. 2017. Genetic screen in drosophila muscle identifies autophagy-mediated T-tubule remodeling and a Rab2 role in autophagy. *Elife* **6**. doi:10.7554/eLife.23367

Grewal SS, Evans JR, Edgar BA. 2007. Drosophila TIF-IA is required for ribosome synthesis and cell growth and is regulated by the TOR pathway. *Journal of Cell Biology* **179**:1105–1113. doi:10.1083/jcb.200709044

Guo T, Nan Z, Miao C, Jin X, Yang W, Wang Z, Tu Y, Bao H, Lyu J, Zheng H, Deng Q, Guo P, YongmeiXi X, Yang X, Ge W. 2019. The autophagy-related gene Atg101 in Drosophila regulates both neuron and midgut homeostasis. *Journal of Biological Chemistry* **294**:5666–5676. doi:10.1074/jbc.RA118.006069

Hashimshony T, Senderovich N, Avital G, Klochendler A, de Leeuw Y, Anavy L, Gennert D, Li S, Livak KJ, Rozenblatt-Rosen O, Dor Y, Regev A, Yanai I. 2016. CEL-Seq2: Sensitive highly-multiplexed single-cell RNA-Seq. *Genome Biol* **17**. doi:10.1186/s13059-016-0938-8

Hegedus K, Nagy P, Gáspári Z, Juhász G. 2014. The putative HORMA domain protein Atg101 dimerizes and is required for starvation-induced and selective autophagy in drosophila. *Biomed Res Int* **2014**. doi:10.1155/2014/470482

Johansen T, Lamark T. 2020. Selective Autophagy: ATG8 Family Proteins, LIR Motifs and Cargo Receptors. *J Mol Biol*. doi:10.1016/j.jmb.2019.07.016

Kamiyama T, Niwa R. 2022. Transcriptional Regulators of Ecdysteroid Biosynthetic Enzymes and Their Roles in Insect Development. *Front Physiol*. doi:10.3389/fphys.2022.823418

Kanki T, Wang K, Cao Y, Baba M, Klionsky DJ. 2009. Atg32 Is a Mitochondrial Protein that Confers Selectivity during Mitophagy. *Dev Cell* **17**:98–109. doi:10.1016/j.devcel.2009.06.014

Karsli-Uzunbas G, Guo JY, Price S, Teng X, Laddha S V., Khor S, Kalaany NY, Jacks T, Chan CS, Rabinowitz JD, White E. 2014. Autophagy is required for glucose homeostasis and lung tumor maintenance. *Cancer Discov.* **4**:915–927. doi:10.1158/2159-8290.CD-14-0363

Kawaguchi K, Fujita N. 2024. Shaping transverse-tubules: central mechanisms that play a role in the cytosol zoning for muscle contraction. *J Biochem*. doi:10.1093/jb/mvad083

Kondo S, Ueda R. 2013. Highly Improved gene targeting by germline-specific Cas9 expression in Drosophila. *Genetics* **195**:715–721. doi:10.1534/genetics.113.156737

Kumar L, Futschik M. 2007. Software Mfuzz: A software package for soft clustering of microarray data. *Bioinformation* **2**:5–7. doi: 10.6026/97320630002005.

Lamark T, Johansen T. 2021. Mechanisms of Selective Autophagy. *Annu Rev Cell Dev Biol 2021* **37**:143–69. doi.org/10.1146/annurev-cellbio-120219-035530 Lee JJ, Sanchez-Martinez A, Zarate AM, Benincá C, Mayor U, Clague MJ, Whitworth AJ. 2018. Basal mitophagy is widespread in Drosophila but minimally affected by loss of Pink1 or parkin. *Journal of Cell Biology* **217**:1613–1622. doi:10.1083/jcb.201801044

Li Y, Zheng W, Lu Y, Zheng Y, Pan L, Wu X, Yuan Y, Shen Z, Ma S, Zhang Xingxian, Wu J, Chen Z, Zhang Xiangnan. 2022. BNIP3L/NIX-mediated mitophagy: molecular mechanisms and implications for human disease. *Cell Death Dis*. doi:10.1038/s41419-021-04469-y

Liang M, Hody C, Yammine V, Soin R, Sun Y, Lin X, Tian X, Meurs R, Perdrau C, Delacourt N, Oumalis M, Andris F, Conrard L, Kruys V, Gueydan C. 2023. eIF4EHP promotes Ldh mRNA translation in and fruit fly adaptation to hypoxia. *EMBO Rep* **24**. doi:10.15252/embr.202256460

Lieber T, Jeedigunta SP, Palozzi JM, Lehmann R, Hurd TR. 2019. Mitochondrial fragmentation drives selective removal of deleterious mtDNA in the germline. *Nature* **570**:380–384. doi:10.1038/s41586-019-1213-4

Lőrincz P, Juhász G. 2020. Autophagosome-Lysosome Fusion. *J Mol Biol*. doi:10.1016/j.jmb.2019.10.028

Mao Q, Acharya A, Rodríguez-Delarosa A, Marchiano F, Dehapiot B, Tanoury Z Al, Rao J, Díaz-Cuadros M, Mansur A, Wagner E, Chardes C, Gupta V, Lenne PF, Habermann BH, Theodoly O, Pourquié O, Schnorrer F. 2022. Tension-driven multi-scale self-organisation in human iPSC-derived muscle fibers. *Elife* **11**. doi:10.7554/eLife.76649

Masiero E, Agatea L, Mammucari C, Blaauw B, Loro E, Komatsu M, Metzger D, Reggiani C, Schiaffino S, Sandri M. 2009. Autophagy Is Required to Maintain Muscle Mass. *Cell Metab.* **10**:507–515. doi:10.1016/j.cmet.2009.10.008

Mcguire SE, Osborn AJ, Davis R. 2004. Temporal and regional gene expression targeting with the conventional GAL4/UAS system in Drosophila.

Morishita H, Mizushima N. 2019. Annual Review of Cell and Developmental Biology Diverse Cellular Roles of Autophagy Autophagosome: a double-membrane structure enclosing cytoplasmic materials. *Annu Rev Cell Dev Biol* **35**:453–75. doi:10.1146/annurev-cellbio-100818

Murakawa T, Kiger AA, Sakamaki Y, Fukuda M, Fujita N. 2020. An autophagy-dependent tubular lysosomal network synchronizes degradative activity required for muscle remodeling. *J Cell Sci* **133**. doi:10.1242/jcs.248336

Murakawa T, Nakamura T, Kawaguchi K, Murayama F, Zhao N, Stasevich TJ, Kimura H, Fujita N. 2022. A Drosophila toolkit for HA-tagged proteins unveils a block in autophagy flux in the last instar larval fat body. *Development (Cambridge)* **149**. doi:10.1242/dev.200243

Nakatogawa H. 2020. Mechanisms governing autophagosome biogenesis. *Nat Rev Mol Cell Biol*. doi:10.1038/s41580-020-0241-0

Narendra DP, Youle RJ. 2024. The role of PINK1–Parkin in mitochondrial quality control. *Nat Cell Biol*. doi:10.1038/s41556-024-01513-9

Ney PA. 2015. Mitochondrial autophagy: Origins, significance, and role of BNIP3 and NIX. *Biochim Biophys Acta Mol Cell Res*. doi:10.1016/j.bbamcr.2015.02.022

Niemi NM, Friedman JR. 2024. Coordinating BNIP3/NIX-mediated mitophagy in space and time. *Biochem Soc Trans*. doi:10.1042/BST20221364

Noda NN, Mizushima N. 2016. Atg101: Not Just an Accessory Subunit in the Autophagy-initiation Complex Mini-review and Review, CELL STRUCTURE AND FUNCTION. https://doi.org/10.1247/csf.15013

Novak I, Kirkin V, McEwan DG, Zhang J, Wild P, Rozenknop A, Rogov V, Löhr F, Popovic D, Occhipinti A, Reichert AS, Terzic J, Dötsch V, Ney PA, Dikic I. 2010. Nix is a selective autophagy receptor for mitochondrial clearance. *EMBO Rep* **11**:45–51. doi:10.1038/embor.2009.256

Okamoto K, Kondo-Okamoto N, Ohsumi Y. 2009. Mitochondria-Anchored Receptor Atg32 Mediates Degradation of Mitochondria via Selective Autophagy. *Dev Cell* **17**:87–97. doi:10.1016/j.devcel.2009.06.013

Onishi M, Yamano K, Sato M, Matsuda N, Okamoto K. 2021. Molecular mechanisms and physiological functions of mitophagy. *EMBO J* **40**. doi:10.15252/embj.2020104705

Palozzi JM, Jeedigunta SP, Minenkova A V., Monteiro VL, Thompson ZS, Lieber T, Hurd TR. 2022. Mitochondrial DNA quality control in the female germline requires a unique programmed mitophagy. *Cell Metab* **34**:1809-1823.e6. doi:10.1016/j.cmet.2022.10.005

Piccirillo R, Demontis F, Perrimon N, Goldberg AL. 2014. Mechanisms of muscle growth and atrophy in mammals and Drosophila. *Developmental Dynamics* **243**:201–215. doi:10.1002/dvdy.24036

Quy PN, Kuma A, Pierres P, Mizushima N. 2013. Proteasome-dependent activation of mammalian target of rapamycin complex 1 (mTORC1) is essential for autophagy suppression and muscle remodeling following denervation. *Journal of Biological Chemistry* **288**:1125–1134. doi:10.1074/jbc.M112.399949

Ribeiro I, Yuan L, Tanentzapf G, Dowling JJ, Kiger A. 2011. Phosphoinositide regulation of integrin trafficking required for muscle attachment and maintenance. *PLoS Genet* **7**. doi:10.1371/journal.pgen.1001295

Sánchez-Martín P, Saito T, Komatsu M. 2019. p62/SQSTM1: 'Jack of all trades' in health and cancer. *FEBS Journal*. doi:10.1111/febs.14712

Sandoval H, Thiagarajan P, Dasgupta SK, Schumacher A, Prchal JT, Chen M, Wang J. 2008. Essential role for Nix in autophagic maturation of erythroid cells. *Nature* **454**:232–235. doi:10.1038/nature07006

Sanger JW, Wang J, Fan Y, White J, Sanger JM. 2010. Assembly and dynamics of myofibrils. *J Biomed Biotechnol*. doi:10.1155/2010/858606

Sartori R, Romanello V, Sandri M. 2021. Mechanisms of muscle atrophy and hypertrophy: implications in health and disease. *Nat Commun*. doi:10.1038/s41467-020-20123-1

Saxton RA, Sabatini DM. 2017. mTOR Signaling in Growth, Metabolism, and Disease. *Cell*. doi:10.1016/j.cell.2017.02.004

Schwarten M, Mohrlüder J, Ma P, Stoldt M, Thielmann Y, Stangler T, Hersch N, Hoffmann B, Merkel R, Willbold D. 2009. Nix directly binds to GABARAP: A possible crosstalk between apoptosis and autophagy. *Autophagy* **5**:690–698. doi:10.4161/auto.5.5.8494

Schweers RL, Zhang J, Randall MS, Loyd MR, Li W, Dorsey FC, Kundu M, Opferman JT, Cleveland JL, Miller JL, Ney PA. 2007. NIX is required for programmed mitochondrial clearance during reticulocyte maturation. *Proc. Natl. Acad. Sci. U.S.A.* **104** (49) 19500-19505. https://doi.org/10.1073/pnas.0708818104

Semenza GL. 2014. Oxygen sensing, hypoxia-inducible factors, and disease pathophysiology. *Annual Review of Pathology: Mechanisms of Disease* **9**:47–71. doi:10.1146/annurev-pathol-012513-104720

Strong LM, Chang C, Riley JF, Boecker CA, Flower TG, Buffalo CZ, Ren X, Stavoe AK, Holzbaur EL, Hurley JH. 2021. Structural basis for membrane recruitment of ATG16L1 by WIPI2 in autophagy. *eLife* 10. doi:10.7554/eLife

Vargas JNS, Hamasaki M, Kawabata T, Youle RJ, Yoshimori T. 2023. The mechanisms and roles of selective autophagy in mammals. *Nat Rev Mol Cell Biol*. doi:10.1038/s41580-022-00542-2

Wang X, Yu L, Wu AR. 2021. The effect of methanol fixation on single-cell RNA sequencing data. *BMC Genomics* **22**. doi:10.1186/s12864-021-07744-6

Yamashita SI, Sugiura Y, Matsuoka Y, Maeda R, Inoue K, Furukawa K, Fukuda T, Chan DC, Kanki T. 2024. Mitophagy mediated by BNIP3 and NIX protects against ferroptosis by downregulating mitochondrial reactive oxygen species. *Cell Death Differ* **31**:651–661. doi:10.1038/s41418-024-01280-y

Yoshii SR, Kuma A, Akashi T, Hara T, Yamamoto A, Kurikawa Y, Itakura E, Tsukamoto S, Shitara H, Eishi Y, Mizushima N. 2016. Systemic Analysis of Atg5-Null Mice Rescued from Neonatal Lethality by Transgenic ATG5 Expression in Neurons. *Dev Cell* **39**:116–130. doi:10.1016/j.devcel.2016.09.001

Zhang J, Loyd MR, Randall MS, Waddell MB, Kriwacki RW, Ney PA. 2012. A short linear motif in BNIP3L (NIX) mediates mitochondrial clearance in reticulocytes. *Autophagy* **8**:1325–1332. doi:10.4161/auto.20764

Zhang S, Wu S, Yao R, Wei X, Ohlstein B, Guo Z. 2024. Eclosion muscles secrete ecdysteroids to initiate asymmetric intestinal stem cell division in Drosophila. *Dev Cell* **59**:125-140.e12. doi:10.1016/j.devcel.2023.11.016

Zhang X, Avellaneda J, Spletter ML, Lemke SB, Mangeol P, Habermann BH, Schnorrer F. 2024. Mechanoresponsive regulation of myogenesis by the force-sensing transcriptional regulator Tono. *Current Biology*. doi:10.1016/j.cub.2024.07.079

Zitserman D, Roegiers F. 2011. Live-cell Imaging of Sensory Organ Precursor Cells in Intact DrosophilaPupae. *Journal of Visualized Experiments*. doi:10.3791/2706

Figure legends

Figure 1. Time-course RNA-seq of the DIOM remodeling in wild-type *Drosophila*

(A) A timeline of DIOM remodeling. Samples were collected at five time points: third instar larva (3IL) and 1 to 4 days after puparium formation (APF). (B) The scheme for sample preparation of DIOMs. Red-colored rectangles indicate single DIOMs. (C) DESeq2 principal component analysis (PCA) of all mRNA-seq libraries. The first four principal components are shown. PC1-2, left; PC3-4, right. The dotted arrow in the PC1-2 plot represents the direction of the transcription dynamics. (D) Heat map of fuzzy c-means cluster core expression profiles. All genes were categorized into twelve clusters. (E) Factor loadings of each cluster to PC1-2 and PC3-4. The circles show r=0.8 (PC1-2) or r=0.7 (PC3-4). (F) GO enrichment at each time point during metamorphosis. The width of each line represents the expression level of the clusters indicated.

Figure 2. Transcriptional dynamics during DIOM remodeling is independent of autophagy

(A) A schematic of DIOM remodeling in wild-type and autophagy-deficient conditions. Autophagy-dependent muscle atrophy starts at 12-14 h APF. (B) Genotypes and time points of the comparative RNA-seq analysis (top) and a diagram of autophagosome formation (bottom). *FIP200* or *Atg18a* RNAi blocks autophagosome formation. *Stx17* RNAi blocks the autophagosome-lysosome fusion. (C) DESeq2 PCA of all mRNA-seq libraries. PC1-2, left; PC3-4, right. A total of 20 samples were analyzed. (D and E) DIOM volume changes in control or *FIP200* RNAi from 3IL to 4 d APF. GFP expression indicates DIOMs. Projected images of XY and XZ planes are shown (D). (E) Relative DIOM cell volume for each genotype normalized to 3IL (set to 1).

Figure 3. Loss of BNIP3 results in accumulation of mitochondria in DIOMs

(A) A schematic of 4 d APF DIOMs in wild-type, *FIP200* RNAi, or *Stx17* RNAi. (B) TEM image of *Stx17* RNAi DIOM at 4 d APF. White arrowheads indicate autophagosome structures. (C) TEM image of wild-type DIOM at 1 d APF. White arrows indicate mitophagosome membrane structure. (D) The expression level of mitophagy regulators in DIOMs at 1 d APF. N=4. Normalized counts in RNA-seq are shown. (E) The expression level of *BNIP3* and *Fbxl4*

in DIOMs. N=4. (F) A diagram illustrating the *BNIP3* knockout strategy, where all exons were deleted using two gRNAs and replaced with a 3xP3-RFP marker. (G) Loss of BNIP3 phenotype on mitochondria and myofibrils in DIOM at 4 d APF.

Figure 4. BNIP3 is required for mitophagosome formation

(A and B) TEM images of DIOM transverse sections at 4 d APF in wild-type (A) or *BNIP3* KO (B). Mitochondria are shown in green. (C and D) TEM images of DIOM transverse sections at 4 d APF in *Stx17* RNAi (C) or a combination of *Stx17* RNAi and *BNIP3* KO (D). Mitophagosomes, pink; Mitochondria, green; autophagosomes, blue. (E) The number of mitophagosomes and mitochondria per unit area in the indicated genotypes. (F) The number of total autophagosomes, including mitophagosomes, per unit area in the indicated genotypes. *Stx17* RNAi, N = 20; *Stx17* RNAi and *BNIP3* KO, N = 17 (Mann-Whitney test) (E and F).

Figure 5. The LIR and MER motifs are required for BNIP3-mediated mitochondrial clearance

(A) Schematics of *Drosophila* BNIP3 and its mutants. (B) GFP pulldown experiment between GFP-BNIP3 and HA-Atg18a in S2 cells. (C) The structure of the BNIP3-Atg18a complex predicted by AlphaFold 3. Top, overview: Atg18a is depicted in white, featuring a β-propeller structure consisting of seven blades, with blades 2 and 3 highlighted in green and pink, respectively. For BNIP3, only residues 29–74 are shown in blue for clarity, with the α-helix spanning residues 42–53 highlighted in yellow. Bottom, close-up view: Amino acids positioned to form intramolecular contacts through their side chains are labeled and represented as sticks, with potential hydrogen bonds shown as dashed lines. (D and D') BNIP3 rescue experiment in DIOMs at 4 d APF. The indicated GFP-tagged BNIP3 constructs and tdTomato-Mito were co-expressed in *BNIP3* KO flies using the GAL4/UAS system (D). A minimum of 50 DIOMs were imaged for quantification (D'). (E) The amount of GFP-BNIP3 in *WT* and *Atg101* KO muscles. The GFP-BNIP3 constructs were expressed by Mef2-GAL4 in *WT* or *Atg101* KO flies. Larval fillets were lysed and subjected to western blotting for GFP.

Figure 6. BNIP3-mediated mitophagy eliminates larval muscle mitochondria during muscle remodeling

(A and A’) Time course microscopy of Mito-GFP and F-actin in control or *BNIP3* KO during DIOM remodeling (A). Mitochondria area per total cell area. For 3IL, control, N = 18; *BNIP3* KO, N = 17. For 1 d APF, control, N = 20; *BNIP3* KO, N= 18 (Mann-Whitney test) (A’). (B) Mitophagy assay using Mito-QC in DIOMs at 1 d APF. Pixel intensity correlation profiles and Spearman's correlation coefficients (R values) are shown. (C, D, and D’) Scheme of the use of GAL80 temperature-sensitive mutants ($GAL80^{ts}$). The animals were raised at 29°C (Restrictive) to induce Mito-GFP expression until mid-3IL, then shifted to 18°C (Permissive) to block expression (C). Mito-GFP and ATP5A immunostaining (total mitochondria) signals in muscles at 3IL or 4 d APF (D). Mito-GFP intensities in muscles at each time point normalized to control (set to 1). For 3IL, control, N = 16; *BNIP3* KO, N = 15. For 1 d APF, control, N = 15; *BNIP3* KO, N= 15 (Mann-Whitney test) (D’). (E) A model of muscle remodeling with or without BNIP3. Loss of BNIP3 leads to mitochondrial accumulation, which disrupts muscle remodeling.

Supplemental figure legends

Figure 1—figure supplement-1. RNA-seq of DIOM remodeling

(A) Heatmap of comparisons for each sample based on correlation coefficients. (B) The contribution ratios (bar) and cumulative contribution ratios (red-colored line) of PC1 to 10 are shown. (C) Fuzzy c-means clustering categorized expressed genes in DIOMs into twelve groups. (D) Violin plot showing the expression level of each cluster, with the number of genes in each cluster indicated at the bottom.

Figure 2—figure supplement-1. Expression levels of Atg18a, FIP200, and Stx17 during DIOM remodeling

(A) Heatmap of comparisons for each sample based on correlation coefficients. (B-D) Expression levels of *Atg18a* (B), *FIP200* (C), and *Stx17* (D) in DIOMs under the indicated conditions. N=4.

Figure 2—figure supplement-2. Effect of autophagy deficiency on transcription of ribosomal RNA and proteins

(A) Time-course analysis of the amount of rRNA during DIOM remodeling in the indicated genotypes. (B and C) Loss of autophagy on the number of nuclei in DIOMs at 3 d APF. Nuclei in DIOMs were stained with Hoechst (B). N=6 (Sidak's test) (C). (D-F) Loss of autophagy on nucleolus volume in DIOMs at 3 d APF. DNA and fibrillarin were stained. XY and XZ planes are shown (D). The nucleolus (E) and nucleus (F) volume were calculated from Z-series images. N=12 (Dunnett's T3 multiple comparisons test). (G) A heatmap of the expression levels of RpLs (left) and RpSs (right) relative to control at each time point.

Figure 3—figure supplement-1. Loss of BNIP3 on mitochondria and myofibrils in DIOMs

YFP-Mito and Phalloidin-Alexa633 (F-actin) staining in DIOMs at 4 d APF in the indicated genotypes.

Figure 5—figure supplement-1. GFP-BNIP3 constructs localize to the outer mitochondrial membrane

(A) Localization of GFP-BNIP3 constructs and mitochondria matrix-targeted tdTomato (tdTomato-Mito) in 3IL muscles. (B) BNIP3 rescue experiment in DIOMs at 4 d APF. The indicated GFP-tagged BNIP3 constructs and tdTomato-Mito were co-expressed in *BNIP3* KO flies using the GAL4/UAS system. Individual fluorescence channels are displayed separately.

Figure 6—figure supplement-1. The impact of BNIP3 knockout on the shape of the DIOM during metamorphosis

(A) Time-course microscopy of mCD8-GFP in dorsal muscles imaged through the cuticle in control and BNIP3 KO animals from 3IL to 4 d APF. (B) Time-course microscopy of Mito-GFP and F-actin in control or *BNIP3* KO during DIOM remodeling. Individual fluorescence channels are displayed separately.

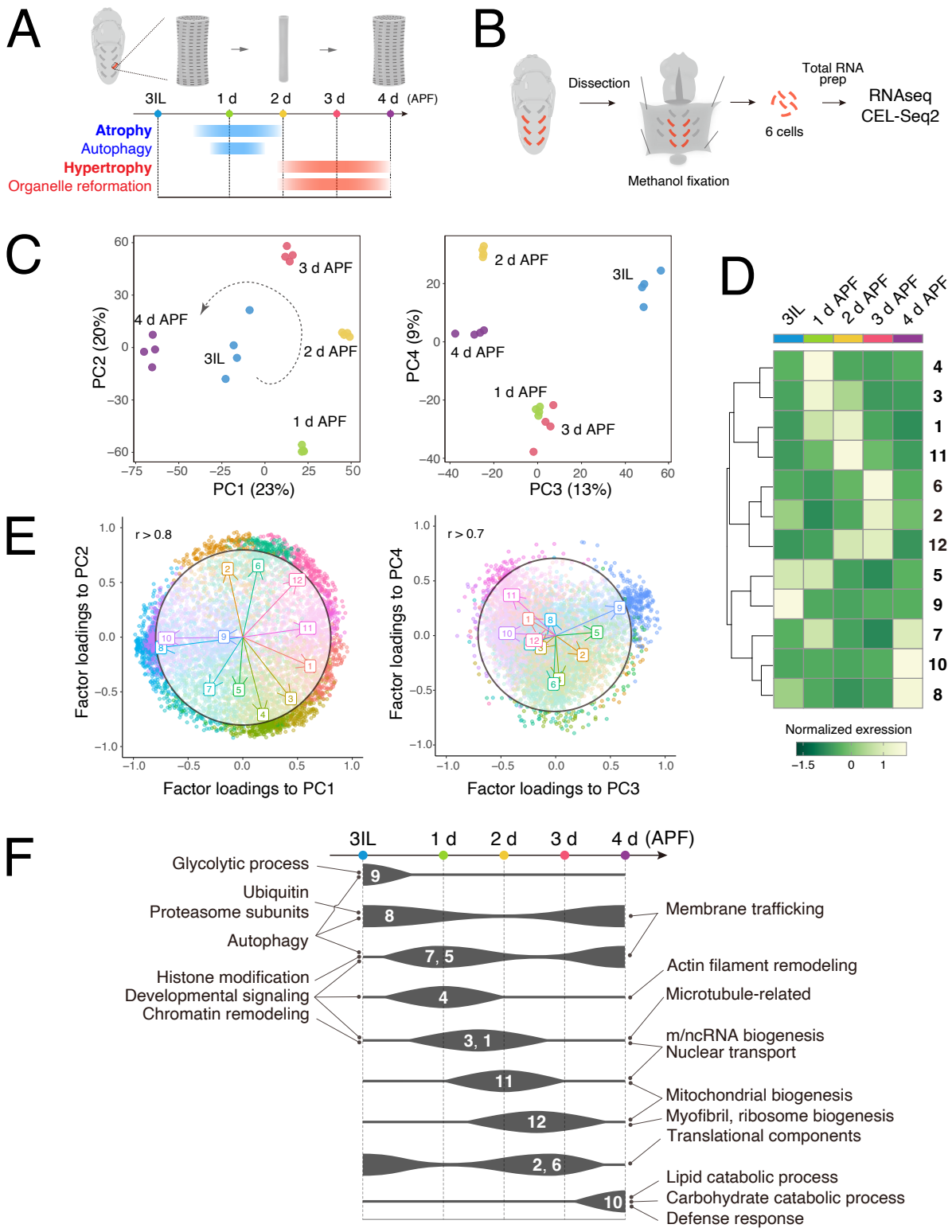

Figure 1. Time-course RNA-seq of the DIOM remodeling in wild-type Drosophila
(A) A timeline of DIOM remodeling. Samples were collected at five time points: third instar larva (3IL) and 1 to 4 days after puparium formation (APF). (B) The scheme for sample preparation of DIOMs. Red-colored rectangles indicate single DIOMs. (C) DESeq2 principal component analysis (PCA) of all mRNA-seq libraries. The first four principal components are shown. PC1-2, left; PC3-4, right. The dotted arrow in the PC1-2 plot represents the direction of the transcription dynamics. (D) Heat map of fuzzy c-means cluster core expression profiles. All genes were categorized into twelve clusters. (E) Factor loadings of each cluster to PC1-2 and PC3-4. The circles show r=0.8 (PC1-2) or r=0.7 (PC3-4). (F) GO enrichment at each time point during metamorphosis. The width of each line represents the expression level of the clusters indicated.

Figure 1

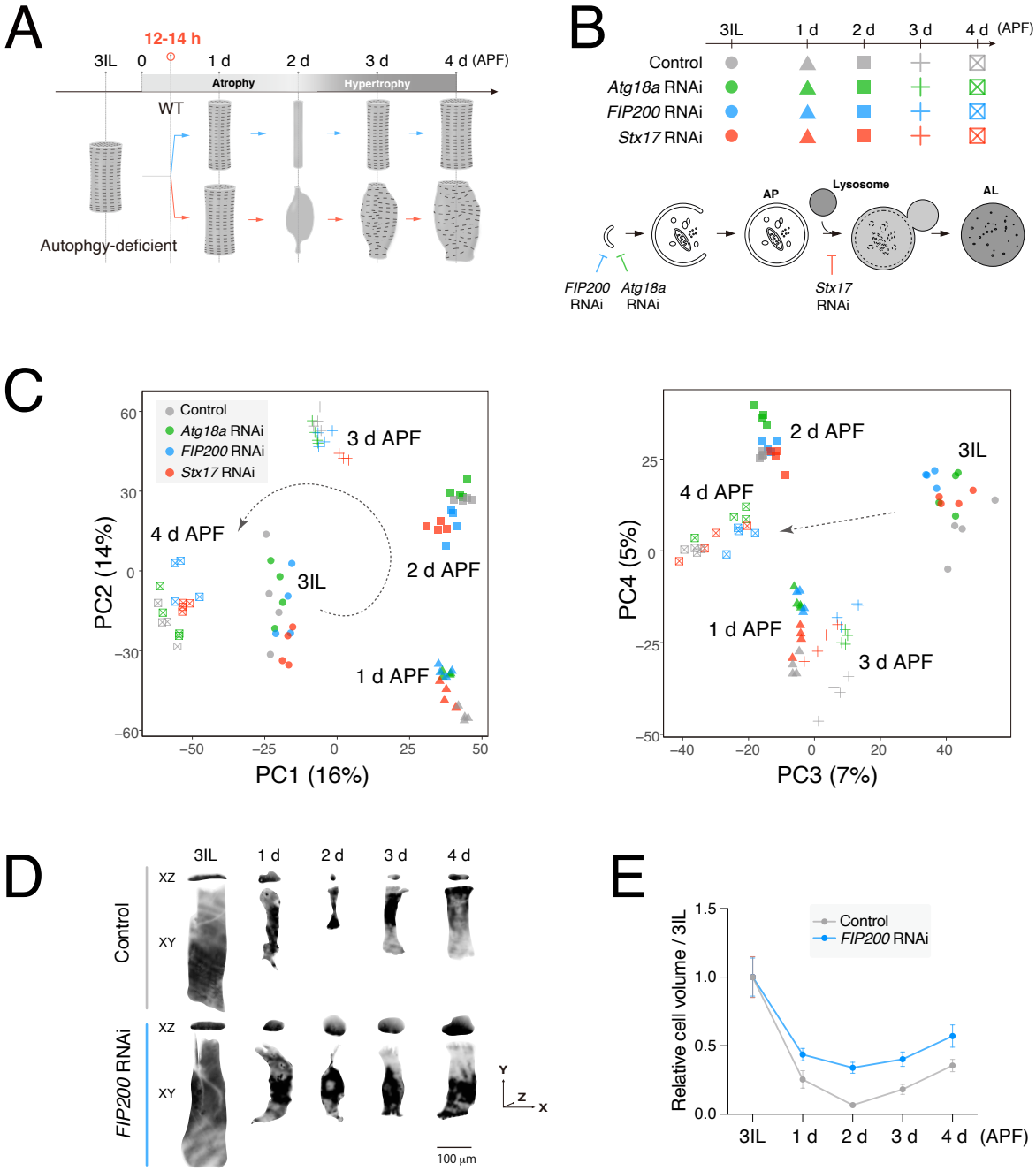

Figure 2. Transcriptional dynamics during DIOM remodeling is independent of autophagy
(A) A schematic of DIOM remodeling in wild-type and autophagy-deficient conditions. Autophagy-dependent muscle atrophy starts at 12-14 h APF. (B) Genotypes and time points of the comparative RNA-seq analysis (top) and a diagram of autophagosome formation (bottom). *FIP200* or *Atg18a* RNAi blocks autophagosome formation. *Stx17* RNAi blocks the autophagosome-lysosome fusion. (C) DESeq2 PCA of all mRNA-seq libraries. PC1-2, left; PC3-4, right. A total of 20 samples were analyzed. (D and E) DIOM volume changes in control or *FIP200* RNAi from 3IL to 4 d APF. GFP expression indicates DIOMs. Projected images of XY and XZ planes are shown (D). (E) Relative DIOM cell volume for each genotype normalized to 3IL (set to 1).

Figure 2

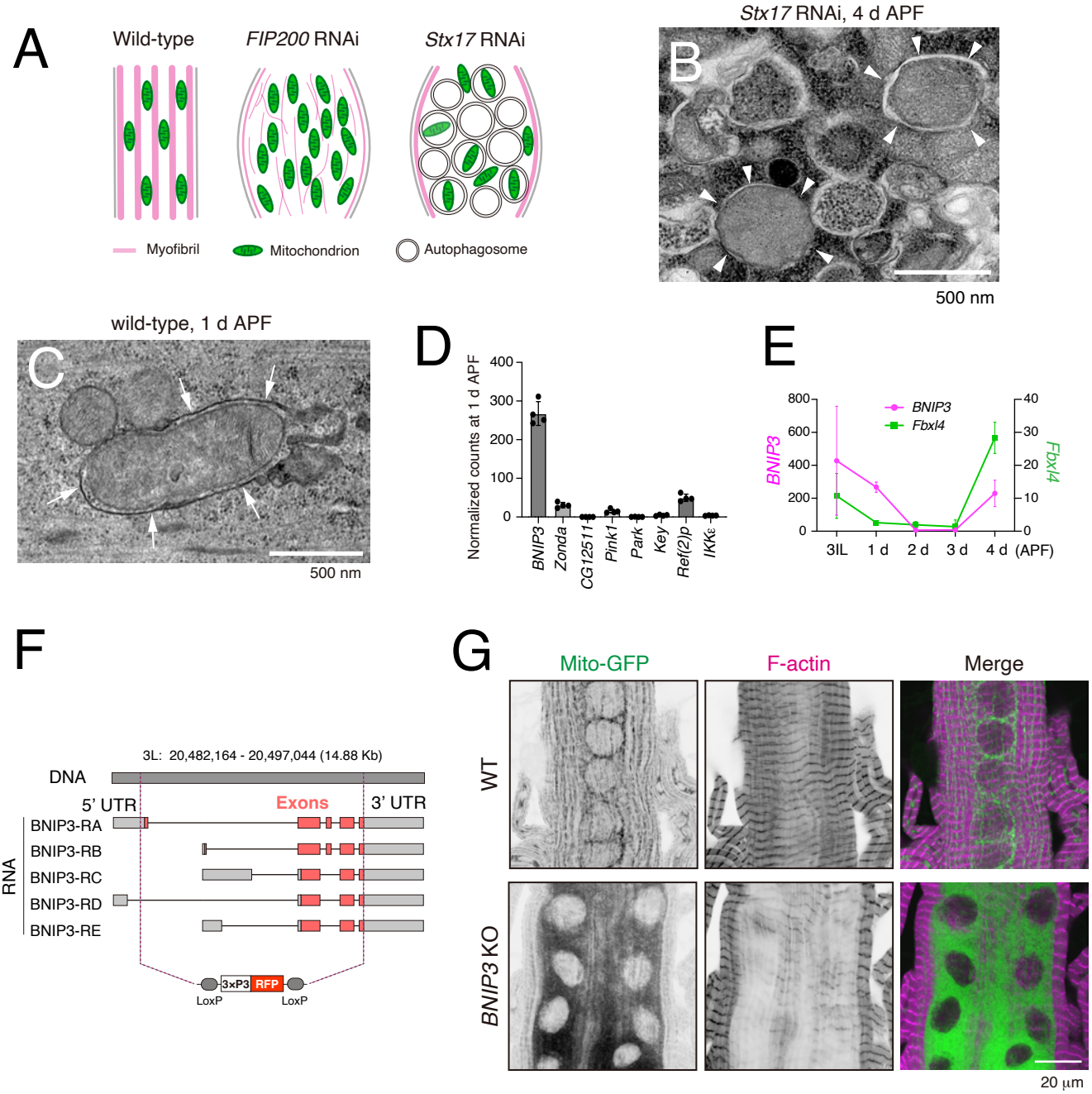

Figure 3. Loss of BNIP3 results in accumulation of mitochondria in DIOMs
(A) A schematic of 4 d APF DIOMs in wild-type, *FIP200* RNAi, or *Stx17* RNAi. (B) TEM image of *Stx17* RNAi DIOM at 4 d APF. White arrowheads indicate autophagosome structures. (C) TEM image of wild-type DIOM at 1 d APF. White arrows indicate mitophagosome membrane structure. (D) The expression level of mitophagy regulators in DIOMs at 1 d APF. N=4. Normalized counts in RNA-seq are shown. (E) The expression level of BNIP3 and Fbxl4 in DIOMs. N=4. (F) A diagram illustrating the *BNIP3* knockout strategy, where all exons were deleted using two gRNAs and replaced with a 3xP3-RFP marker. (G) Loss of BNIP3 phenotype on mitochondria and myofibrils in DIOM at 4 d APF.

Figure 3

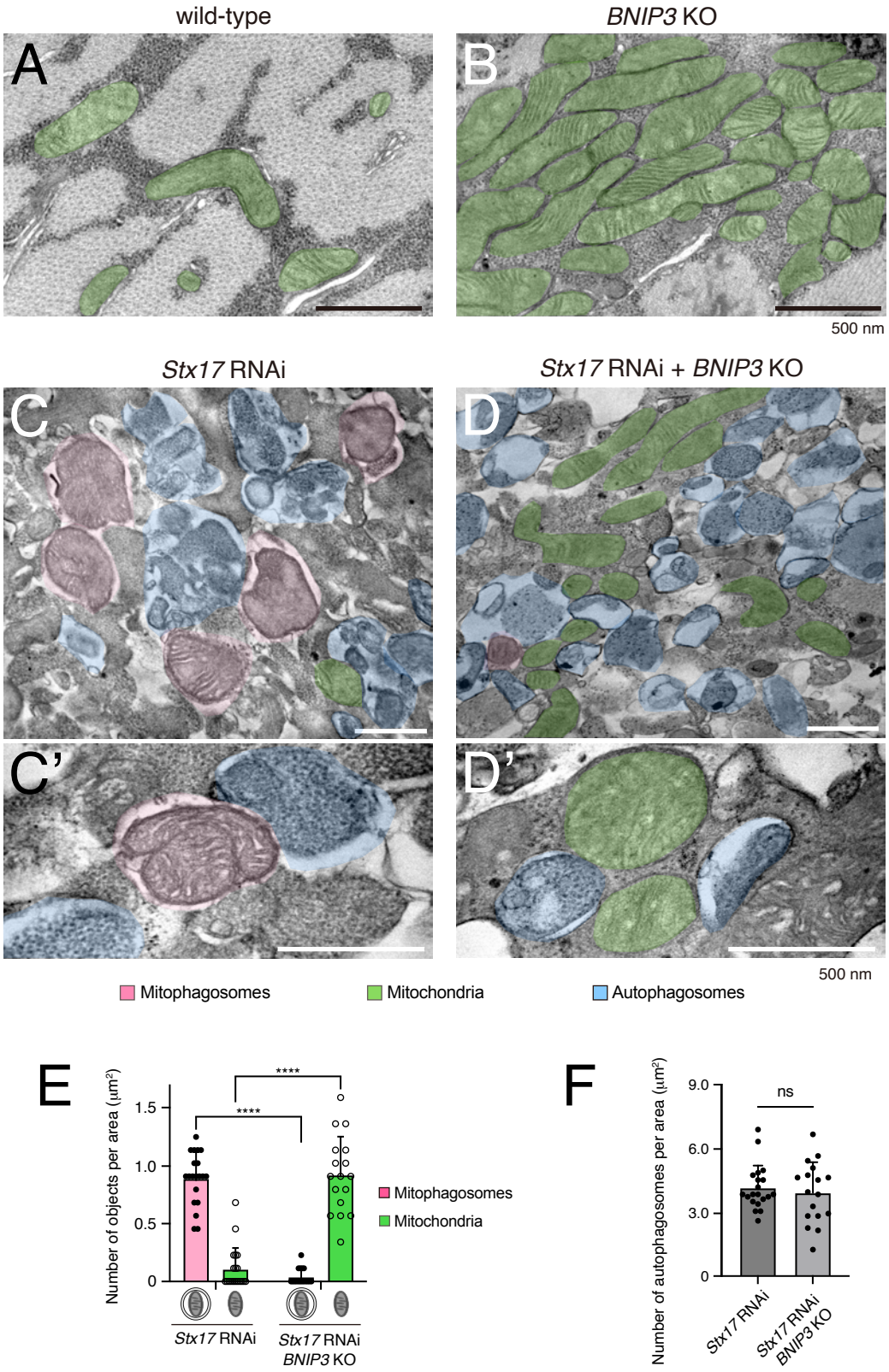

Figure 4. BNIP3 is required for mitophagosome formation
(A and B) TEM images of DIOM transverse sections at 4 d APF in wild-type (A) or *BNIP3* KO (B). Mitochondria are shown in green. (C and D) TEM images of DIOM transverse sections at 4 d APF in *Stx17* RNAi (C) or a combination of *Stx17* RNAi and *BNIP3* KO (D). Mitophagosomes, pink; Mitochondria, green; autophagosomes, blue. (E) The number of mitophagosomes and mitochondria per unit area in the indicated genotypes. (F) The number of total autophagosomes, including mitophagosomes, per unit area in the indicated genotypes. *Stx17* RNAi, N = 20; *Stx17* RNAi and *BNIP3* KO, N = 17 (Mann-Whitney test) (E and F).

Figure 4

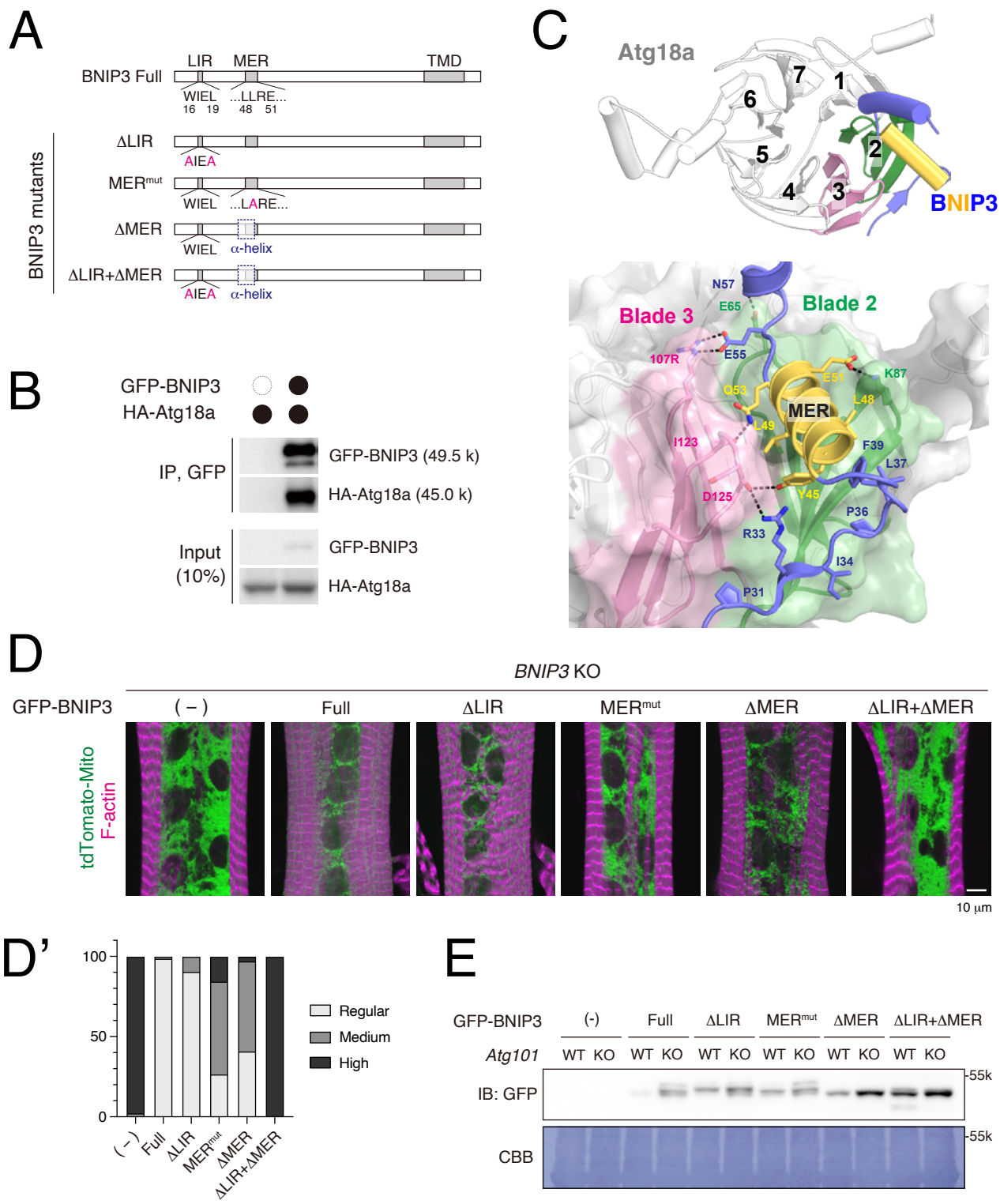

Figure 5. The LIR and MER motifs are required for BNIP3-mediated mitochondria clearance
(A) Schematics of Drosophila BNIP3 and its mutants. (B) GFP pulldown experiment between GFP-BNIP3 and HA-Atg18a in S2 cells. (C) The structure of the BNIP3-Atg18a complex predicted by AlphaFold 3. Top, overview: Atg18a is depicted in white, featuring a β-propeller structure consisting of seven blades, with blades 2 and 3 highlighted in green and pink, respectively. For BNIP3, only residues 29–74 are shown in blue for clarity, with the α-helix spanning residues 42–53 highlighted in yellow. Bottom, close-up view: Amino acids positioned to form intramolecular contacts through their side chains are labeled and represented as sticks, with potential hydrogen bonds shown as dashed lines. (D and D') BNIP3 rescue experiment in DIOMs at 4 d APF. The indicated GFP-tagged BNIP3 constructs and tdTomato-Mito were co-expressed in *BNIP3* KO flies using the GAL4/UAS system (D). A minimum of 50 DIOMs were imaged for quantification (D'). (E) The amount of GFP-BNIP3 in WT and *Atg101* KO muscles. The GFP-BNIP3 constructs were expressed by Mef2-GAL4 in WT or *Atg101* KO flies. Larval fillets were lysed and subjected to western blotting for GFP.

Figure 5

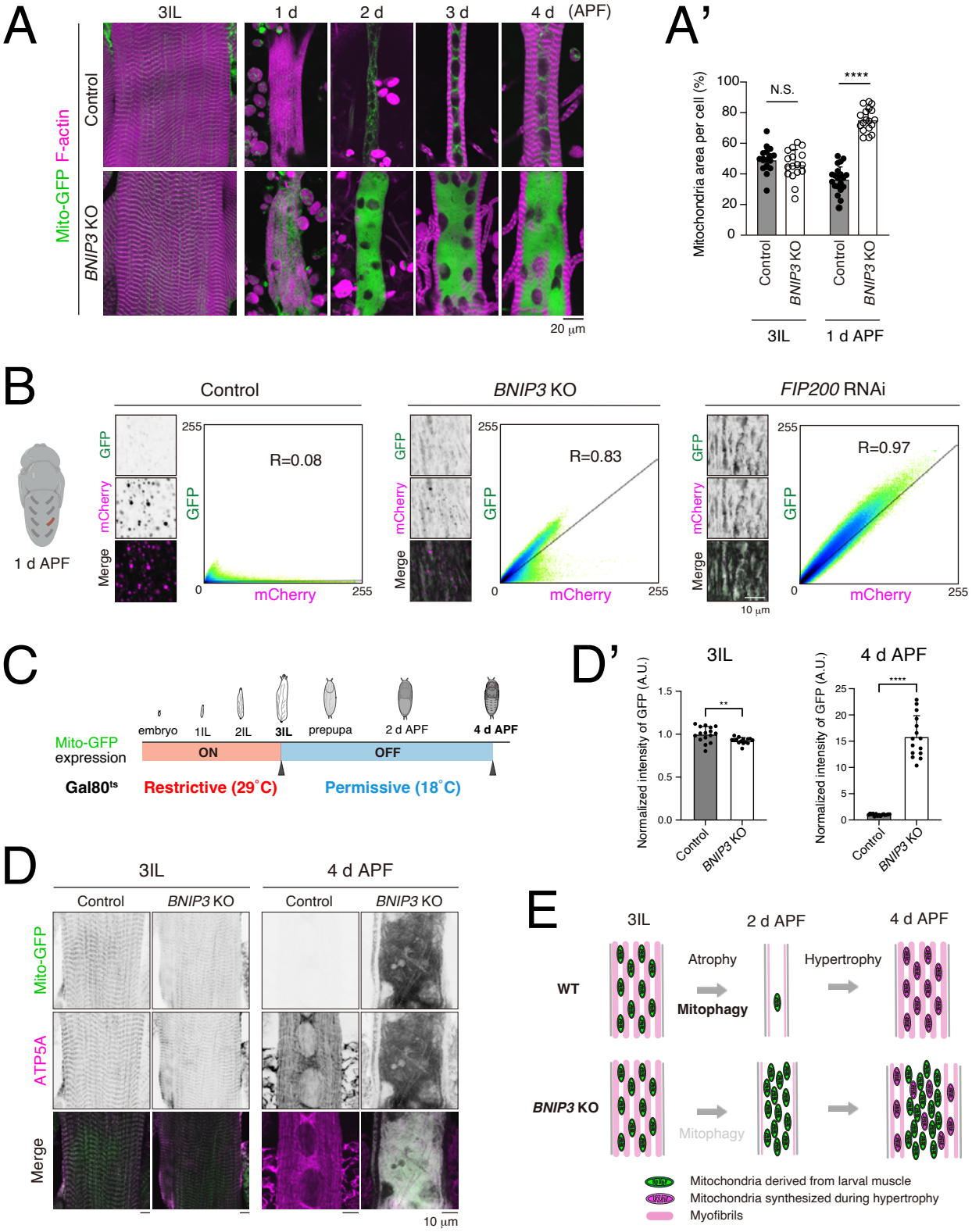

Figure 6. BNIP3-mediated mitophagy eliminates larval muscle mitochondria during muscle remodeling
(A and A') Time course microscopy of Mito-GFP and F-actin in control or *BNIP3* KO during DIOM remodeling (A). Mitochondria area per total cell area. For 3IL, control, N = 18; *BNIP3* KO, N = 17. For 1 d APF, control, N = 20; *BNIP3* KO, N= 18 (Mann-Whitney test) (A'). (B) Mitophagy assay using Mito-QC in DIOMs at 1 d APF. Pixel intensity correlation profiles and Spearman's correlation coefficients (R values) are shown. (C, D, and D') Scheme of the use of GAL80 temperature-sensitive mutants (GAL80^{ts}). The animals were raised at 29°C (Restrictive) to induce Mito-GFP expression until mid-3IL, then shifted to 18°C (Permissive) to block expression (C). Mito-GFP and ATP5A immunostaining (total mitochondria) signals in muscles at 3IL or 4 d APF (D). Mito-GFP intensities in muscles at each time point normalized to control (set to 1). For 3IL, control, N = 16; *BNIP3* KO, N = 15. For 1 d APF, control, N = 15; *BNIP3* KO, N= 15 (Mann-Whitney test) (D'). (E) A model of muscle remodeling with or without BNIP3. Loss of BNIP3 leads to mitochondrial accumulation, which disrupts muscle remodeling.

Figure 6